

## Identification of new classical Be stars from the LAMOST MRS survey

LUQIAN WANG,<sup>1</sup> JIAO LI,<sup>2</sup> YOU WU,<sup>2</sup> DOUGLAS R. GIES,<sup>3</sup> JIN ZHONG LIU,<sup>4,5</sup> CHAO LIU,<sup>2</sup>  
YANJUN GUO,<sup>1,6</sup> XUEFEI CHEN,<sup>1,7</sup> AND ZHANWEN HAN<sup>1,7</sup>

<sup>1</sup>Yunnan Observatories, CAS, P.O. Box 110, Kunming 650011, Yunnan, China

<sup>2</sup>Key Laboratory of Space Astronomy and Technology, National Astronomical Observatories,  
Chinese Academy of Sciences  
Beijing 100101, China

<sup>3</sup>Center for High Angular Resolution Astronomy and Department of Physics and Astronomy,  
Georgia State University, P.O. Box 5060  
Atlanta, GA 30302-5060, USA

<sup>4</sup>Xinjiang Astronomical Observatory, Chinese Academy of Sciences, People's Republic of China

<sup>5</sup>School of Astronomy and Space Science, University of Chinese Academy of Sciences, Beijing 100049, People's  
Republic of China

<sup>6</sup>School of Astronomy and Space Science, University of Chinese Academy of Sciences,  
Beijing 100049, China

<sup>7</sup>Center for Astronomical Mega-Science, Chinese Academy of Science,  
Beijing 100012, China

### ABSTRACT

Be stars are B-type main-sequence stars that display broad Balmer emission lines in their spectra. Identification of Be population is essential to further exam the formation and evolutionary models. We report the detection of classical Be (CBe) stars from observations with the Large sky Area Multi-Object fiber Spectroscopic Telescope Medium Resolution Survey of Date Release 7 (LAMOST MRS DR7). We used a deep convolutional neural network, the **ResNet** with an 18-layer module to examine the morphology of the H $\alpha$  profile. We identified 1,162 candidate Be stars from the collection of 2,260,387 spectra for 789,918 stars in the database. The **ResNet** network achieves a Be star classification accuracy of 99.5%. Among the detections, 151 of these are prior known Be stars cross-matched from the literature. By applying a three-step test, we identified 183 new CBe stars. We find that 41 CBe stars are members of known open clusters. Based upon an investigation of the kinematics of the identified CBe stars from the *Gaia* EDR3 astrometric solutions, we identified 16 new runaways. These new identifications will provide as a reference for future follow-ups to further investigate their physical properties.

*Keywords:* stars: early-type – stars: emission-line, Be – surveys

## 1. INTRODUCTION

Be stars are B-type main-sequence stars, and their optical spectra display or have displayed Balmer emission features that are formed in a decretion circumstellar disk around the star. Based on a study from optical interferometric and spectropolarimetric observations for a sample of seven Be stars by [Quirrenbach et al. \(1997\)](#), they suggest that the disks are geometric thin. The disk is now widely accepted as moving in a Keplerian motion and governed by viscosity ([Rivinius et al. 2013](#)). [Lee et al. \(1991\)](#) proposed the viscous decretion disk model and suggested that materials are ejected from the central star to form a decretion circumstellar disk as a result of outward transferring angular momentum. Observational works conducted in multi-wavelength regimes have successfully corroborated the disk properties as predicted by the model. Examples include a combination of photometric and spectroscopic study spans from near-UV to mid-IR to investigate the disk evolution of  $\omega$  CMa ([Ghoreyshi et al. 2021](#)), the investigation of the disk density distribution and disk mass decretion rates for 80 Be stars from the infrared disk continuum emission ([Vieira et al. 2017](#)), and radio observations for 57 Be stars carried out by [Klement et al. \(2019\)](#) to monitor the spectral energy distribution of the disks.

The portrait illustrates the formation mechanism for the Be phenomenon is far from complete, many formation scenarios have been suggested to fulfill the missing gaps, these include the rapid rotation, non-radial pulsation, and magnetic fields. Be stars are rapidly rotating stars, and their projected rotational velocities can reach up to  $\sim 80\%$  of their critical rotational velocities ([Rivinius et al. 2013](#)). The origin of the rapid rotation of Be stars is still not fully understood, and growing evidence suggests that the rapid rotation is the result of mass and angular momentum accretion in a post, close binary interaction. The detections of Be stars with a compact companion are reported by several works, such as Be X-ray binary systems consisting of a neutron star companion ([Reig 2011](#)), and a Be and stellar-mass black hole binary ([Casares et al. 2014](#)). At the low mass companion end, Be binary systems containing an evolved subdwarf companion have recently been detected through FUV spectroscopic investigations ([Peters et al. 2008, 2013, 2016](#); [Wang et al. 2018, 2021](#)). Kinematics studies of Be stars from [Berger & Gies \(2001\)](#) and [Boubert & Evans \(2018\)](#) suggest that most of them are products of binary systems that have gone through past mass transfer.

Many Be stars often show short-term variability and periodicity from spectroscopic and photometric observations. Non-radial pulsation and presence of magnetic fields may also link to the Be phenomenon ([Rivinius et al. 2013](#)). [Semaan et al. \(2011, 2013\)](#) analyzed the light curves for Be stars in the CoRoT fields and reported that all Be stars are pulsators displaying multi-periodicities. The pulsation is also related to the circumstellar activities, such as disk build-ups, dissipation, and outburst ([Štefl et al. 2003](#); [Richardson et al. 2021](#)). The presence of magnetic fields has also been suggested to account for the spectroscopic and photometric variabilities and modulations in Be stars. Theoretical models, such as the magnetically torqued disk model by [Brown et al. \(2004\)](#) suggests that the magnetic fields may be accounted for the stellar wind mass loss and angular momentum transferring from the central star to the disk, and the magnetic rotator model by [Maheswaran \(2003\)](#) argues that the magnetic fields may be responsible for the formation of the Be Keplerian disk. However, no large-scale magnetic fields have been observed yet, and weak magnetic fields were reported only in a few Be stars ([Hubrig et al. 2006, 2009](#)). Be stars are great laboratories for studying disk physics, such as disk formation and evolutionary processes. They are testbeds for investigating the star-disk

interaction process. Identification for the Be population in the Galaxy is also helpful to constrain the models of formation channels for these rapidly rotating early-type stars (Shao & Li 2014).

Since the spectrographic observations of Be stars by Struve (1931), many searches for Be stars have been carried out through photometric or spectroscopic measurements of their emission features. Jaschek & Egret (1982) compiled a catalog of Galactic 1,159 Be stars from various literature. Witham et al. (2008) presented a catalog of 4,853 H $\alpha$  emission point sources from the INT Photometric H $\alpha$  Survey using the Wide Field Camera (IN/TWFC) for the Northern Galactic Plane (IPHAS), and a later assessment conducted by Gkouvelis et al. (2016) suggests that about 70% of the emission-line objects are classical Be stars (CBe). Utilizing the data from the Very Large Telescope Survey Telescope Photometric H $\alpha$  Survey (VPHAS+), Mohr-Smith et al. (2017) found a total of 14,900 massive OB stars in the Carina Arm region. Aidelman et al. (2020) applied a neural network approach to classify 248 CBe stars from this database. Also, using different machine learning classifiers, Pérez-Ortiz et al. (2017) identified 50 CBe candidate stars in the outskirts of the Large Magellanic Cloud from the Optical Gravitational Lensing Experiments (OGLE) *I*-band light curves. Recently, Vioque et al. (2020) applied a machine-learning approach to search for new Herbig Ae/Be stars using the photometric data from *Gaia* DR2. As a side product, they also reported the detection of 693 newly classified candidate CBe stars distributed over the Galactic plane. The Be Star Spectra (BeSS) database (Neiner et al. 2011) is a continuously updated spectral library contributed from both amateur and professional communities, and it contains optical spectra for about 2,000 CBe stars residing in the Milky Way and Magellanic Clouds (at the time of writing). Based upon observations made from the large surveys, such as the Apache Point Galactic Evolution Experiment (APOGEE), Chojnowski et al. (2015) reported detections of 128 newly found CBe stars. Thanks to the large field-of-view of the Large sky Area Multi-Object fiber Spectroscopic Telescope (LAMOST), Lin et al. (2015) reported the detection of 192 Galactic CBe candidate stars based upon the low-resolution spectra from the DR1, and Hou et al. (2016) reported the discovery of 5,603 new CBe stars from the DR2.

Motivated by the recent release of a large collection of spectroscopic observations from the LAMOST DR7, we are interested in identifying CBe stars from this large and homogeneous database. Here we report our work of using a deep convolutional neural network approach to classify CBe stars from the Data Release 7 of the medium-resolution spectra database. The structure of this work is as follows. We report the data collected from the LAMOST medium resolution survey in Section 2. In Section 3, we describe the procedures to select the early type OB stars from the DR7 database. We report the details for applying the deep convolutional neural network method ResNet to classify Be candidate stars and describe their morphological features in Section 4. The work of identification of CBe stars from the preliminary Be candidate sample is discussed in Section 5. In Section 6, we discuss the membership of identified CBe stars in known open clusters and present the analysis of identifying runaway CBe stars in the sample based on their kinematics. We summarize our work in Section 7.

## 2. LAMOST MRS OPTICAL SPECTROSCOPY

We obtained the optical spectra from the LAMOST at the Xinlong station of the National Astronomical Observatory. The LAMOST, also known as the Guoshoujing Telescope, is a 4 m quasi-meridian reflecting Schmidt telescope with an installment of 4,000 fibers within the 5 deg of Field of View. Starting in 2017, in addition to the existing low-resolution spectrographs ( $R = 1,800$ ), new medium-resolution spectrographs with a resolving power of  $R = 7,500$  were added to the tele-

scope. LAMOST began the new five-year Medium Resolution Survey (MRS) in 2018 October. Part of the observing strategy for this survey is monitoring stars through multi-epoch observations. The LAMOST-MRS spectra are made with blue and red cameras. The spectra cover a wavelength range of 4950–5350 Å for the blue arm and 6300–6800 Å for the red arm (Liu et al. 2020). In order to identify Be stars from the current released MRS database, we downloaded a total collection of 2,260,387 spectra with a signal-to-noise (S/N) greater than 10 per pixel in both blue and red bands from the LAMOST Data Release 7<sup>1</sup>. The targets are brighter than the limiting magnitude of *Gaia*  $G = 14.0$  mag for the selected spectral S/N criterion. The observations were made on nights between 2018 October and 2019 June.

The spectra were reduced and the wavelength calibration was performed following the standard LAMOST 2D pipeline (Luo et al. 2015; Ren et al. 2021). Because cosmic rays were not fully removed by the pipeline, we adopted the Python package `lapsec`<sup>2</sup> from Zhang et al. (2021) to remove any residual cosmic ray features present in the spectra. In order to rectify the observed spectra, we then transformed the spectra of the individual stars onto a uniform wavelength grid and rectified the spectra through a spline fitting to the selected pseudo continuum regions. In Figure 1, we show the spectra of a known Be star J060334.97+221938.6 (HD 250854) observed in both the blue and red bands (black) on the top panels, and the spline fits for each spectrum are shown in red. The rectified spectrum from each arm is shown on the bottom panels and now has a continuum value about unity. The final working product is a matrix of normalized flux, wavelength grid, and the observational dates recorded in the unit of the Modified Julian Date (MJD).

<sup>1</sup> <http://dr7.lamost.org/>

<sup>2</sup> <https://github.com/hypergravity/laspec>

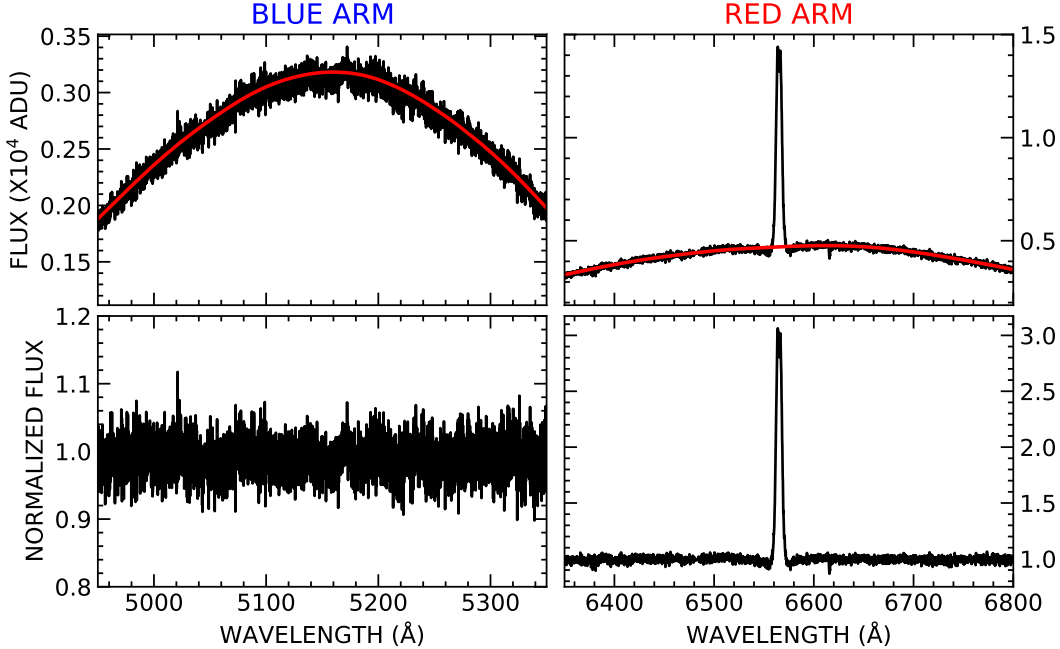


**Figure 1.** The spectra for Be star HD 250854 (with LAMOST designation of J060334.97+221938.6) observed in both blue and red arms from LAMOST are shown in black on the top panels. The spline fits for the spectrum recorded in each arm are shown in red. The rectified spectrum for each band is shown in the bottom panel and has a continuum value about unity.

### 3. SELECTION OF EARLY-TYPE STARS FROM THE MRS DATABASE

The archived spectra from the LAMOST MRS library comprise a broad range of stellar objects. The major goal of this work is to identify CBe stars from the database. We selected the spectra of early-type stars from the archived sample following the procedures described in Guo et al. (2021). We first adopted the estimated effective temperatures ( $T_{\text{eff}}$ ) as given by the LAMOST stellar parameter pipeline (*LASP*, Wu et al. 2014) to coarsely eliminate any late A-type to late F-type stars with  $6,500 \text{ K} \leq T_{\text{eff}} \leq 8,000 \text{ K}$  from the MRS sample. This procedure narrows our initial working sample of 2,260,387 spectra down to 286,501. In order to remove any hidden late-type stars in the sample, we then adopted line profiles that are sensitive to the effective temperature, including  $\text{H}\alpha$   $\lambda 6565$  and Mg I  $b$  triplet ( $\sim \lambda 5200$ ) series to compute their associated equivalent widths ( $EW$ ) to form a distribution of  $EW$  over the selected line indices. The  $EW$  values for  $\text{H}\alpha$   $\lambda$  profile were measured over a wavelength range of  $6548 \sim 6578 \text{ \AA}$  (Cohen et al. 1998) and a bandpass of  $5160 \sim 5193 \text{ \AA}$  was selected for Mg I  $b$  triplet ( $\sim \lambda 5200$ ) series (Worthey et al. 1994). In Figure 2, we show the distribution of measured  $EW$  values for both line profiles in the black cross. Metallic profiles develop their line strength towards late-type stars (Gray & Corbally 2009), we thus retained a sample of 261,647 early-type stellar spectra by keeping stars with measured  $EW < 10.0$  for  $\text{H}\alpha$   $\lambda 6565$  and  $EW < 1.2$  for Mg I  $b$  triplet (the black cross shown on Figure 2 under the red horizontal solid line). Because stars with estimated  $T_{\text{eff}} < 3,100 \text{ K}$  are not given by the *LASP* (Wu et al. 2011; Luo et al. 2015), we further excluded any K- and M-type stars were appearing in the sample from their position in a color-color magnitude plot using the IR photometric observations. Comerón et al. (2002) utilized

the  $J$ -,  $H$ -, and  $K_s$  photometric measurements for stars from the *2MASS* all-sky survey to create an intrinsic color-color diagram to separate early-type and late-type stars in the Cygnus OB2 association (see their Figure 2), they further defined a reddening-free parameter of  $Q = (J - H) - 1.70(H - K_s)$  and reported that early-type stars have typical  $Q$  values about 0, while  $Q = 0.4 - 0.5$  for K- and M-type stars (Comerón & Pasquali 2005; Negueruela & Schurch 2007). We cross-matched the stars in the sample with the *2MASS* database (Cutri et al. 2003) using a circular searching aperture of  $3''$  to collect their photometric measurements, and we calculated the associated  $Q$  values. By adopting the  $Q$  criterion, we rejected 3,787 spectra for any K- and M-type stars appearing in the sample (shown as the blue cross in Figure 2). The working sample is a collection of 257,860 early-type stellar spectra.

#### 4. IDENTIFICATION OF $H\alpha$ EMISSION STARS FROM LAMOST MRS SPECTRA

A broad range of astrophysical objects displays  $H\alpha$  emission features in their spectra. Examples include planetary nebulae objects, in which the emission feature originates from the ionized hydrogen gas at the ending stage of the stellar evolution of low-mass stars. Emission is also present in the spectra of pre-main-sequence young stellar objects, such as Herbig Ae/Be stars. Early-type main-sequence emission line stars, such as Oe, Be, or Ae stars, display  $H\alpha$  emission features that are likely formed from the stellar wind or a decretion disk. In order to identify Be stars from the MRS database, we initiated a deep convolutional neural network approach to form a preliminary list of Be candidate stars from the identified early-type stars as described in Section 3.

##### 4.1. Preliminary selection of Be stars from the ResNet

In recent years, machine learning techniques have been widely used to classify different types of astronomical images and signals based upon an automatic representation learning approach, such as the traditional kernel methods and deep Convolutional Neural Network (CNN) learning input data through the usage of multiple layers. The classification task is achieved by minimizing the generalization errors for the learning process, and the learning techniques differ in performance by their convergence rate to perform the recognition task.

As described in Lecun et al. (2015), layers are applied to given input data to learn the morphological features from the data themselves. The output from each layer is evaluated by weighting factors to score the performance of the learning module from the desired recognition score, and subsequent layers learn from the input to identify classes in such a way to minimize the recognition errors. Outputs from the layers are combined to assemble the final representation of the identity. This technique is particularly efficient in identifying observational images with arrays of pixels in the modern large data era.

The representation of an identity learned from CNN benefits from gaining higher accuracy by adding more layers to the neural network architecture. Simply stacking more layers to the architecture may encounter a degradation issue, in which the accuracy of the recognition task reaches saturation and starts to decline (He et al. 2016a). We can reduce the computing time budget of applying CNN to a large set of images by combining the residual learning module with shortcut connections (the ResNet algorithm), in which a layer or multiple layers are skipped to proceed with the identity mapping (see Figure 2 in He et al. 2016b). A detailed description of the building blocks and connection skipping are discussed in He et al. (2016a).

Compared to the traditional image classification approach, such as the kernel method, the ResNet algorithm achieves higher accuracy and maintains a faster converging rate. Allen-Zhu & Li (2019)



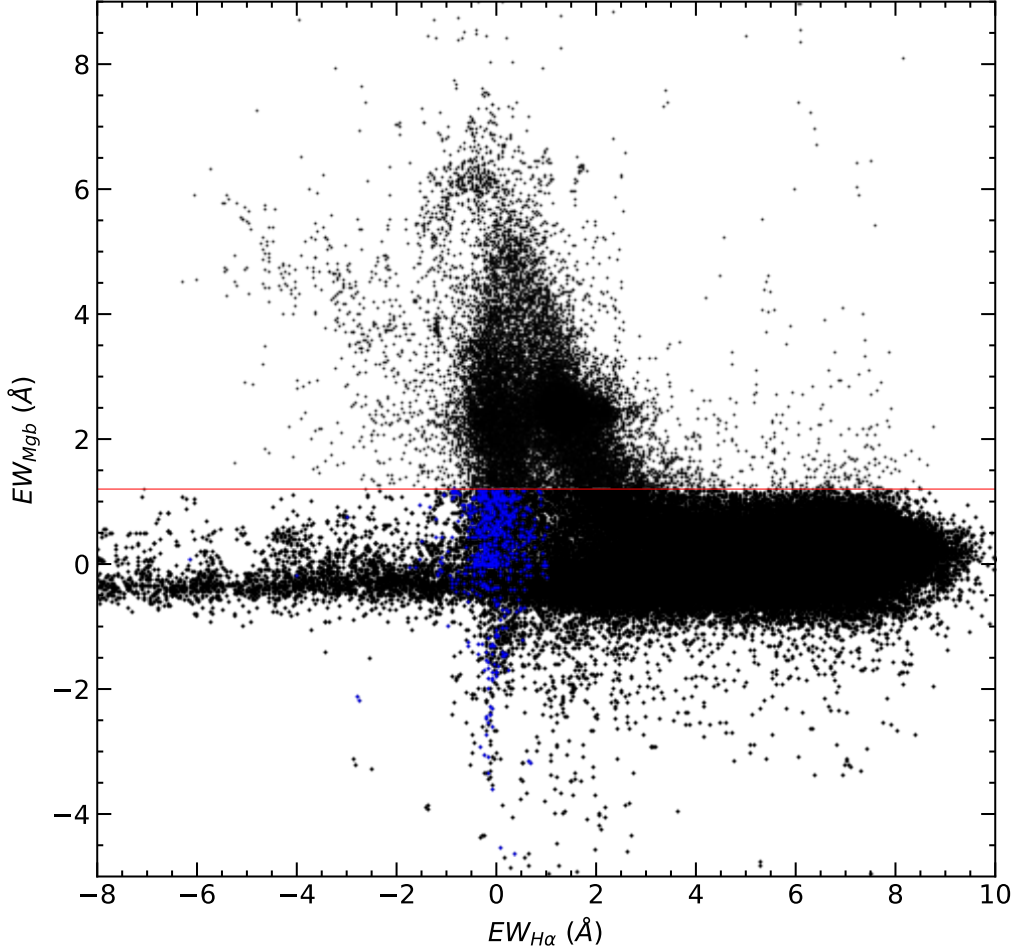


**Figure 2.** The distribution of measured  $EW$  values for 286,501 spectra from H $\alpha$   $\lambda$ 6565 and Mg I  $b$  triplet ( $\sim \lambda$ 5200) are shown in black cross. A sample of 261,647 early-type stellar spectra were retained by keeping stars with measured  $EW < 10.0$  for H $\alpha$   $\lambda$ 6565 and  $EW < 1.2$  for Mg I  $b$  triplet (the black cross under the red horizontal solid line). By applying a reddening-free parameter from Comerón & Pasquali (2005) using observations obtained from the 2MASS all-sky survey, we further rejected 3,787 K- and M-type stars in the sample (blue cross). Our final working sample narrows down to a collection of 257,860 early-type stellar spectra.

investigates the performance of these image classification schemes and provides provable evidence showing that the ResNet reduces the complexity of training sample through the use of the multiple layers compared to the traditional “one-shot” learning algorithm, and thus improves the classification efficiency. Also, smaller generalization errors were obtained from the ResNet algorithms. For the same input data, traditional kernel methods can reach classification accuracy of 77%–85%, while the ResNet achieves an accuracy of 96% (Recht et al. 2018; Arora et al. 2019).

The **ResNet** algorithm has been successfully applied to many astronomical image identification tasks. [Li et al. \(2019\)](#) applied the **ResNet** module to search for potential galaxy Ly $\alpha$  emitter gravitational lens candidates from the SDSS III spectroscopy survey. The **ResNet** code was used to select pulsar candidates from the billion-scale database of the radio survey from the Five-hundred-meter Aperture Spherical radio Telescope ([Wang et al. 2019](#)). [Zhu et al. \(2019\)](#) adopted several CNN variant networks to classify 28,790 galaxy images into five classes based upon the morphological features of the galaxies from the Galaxy Zoo 2 database, and they concluded that the variant **ResNet** model achieved state-of-art classification performance among the selected networks. There is a large collection of H $\alpha$  emission stars among those from the LAMOST MRS DR7, so we adopted this deep convolutional residual network to identify Be candidate stars in the database.

In this work, we used the 18-layer **ResNet** to identify Be star candidate stars in the sample. The **ResNet** learning module was implemented in *torchvision.models*<sup>3</sup> and obtained from the deep learning library of *PyTorch 1.9.0* ([Paszke et al. 2019](#)). The loss function of cross-entropy loss was adopted for the training, and the Adam optimizer from [Kingma & Ba \(2014\)](#) was used to optimize the training model. We adopted a dynamic learning rate scheduler with an initial learning rate of 0.001. To improve the performance of the model and reduce the training epochs, the weights we loaded to the module were pre-trained on the *ImageNet* ([Deng et al. 2009](#)).

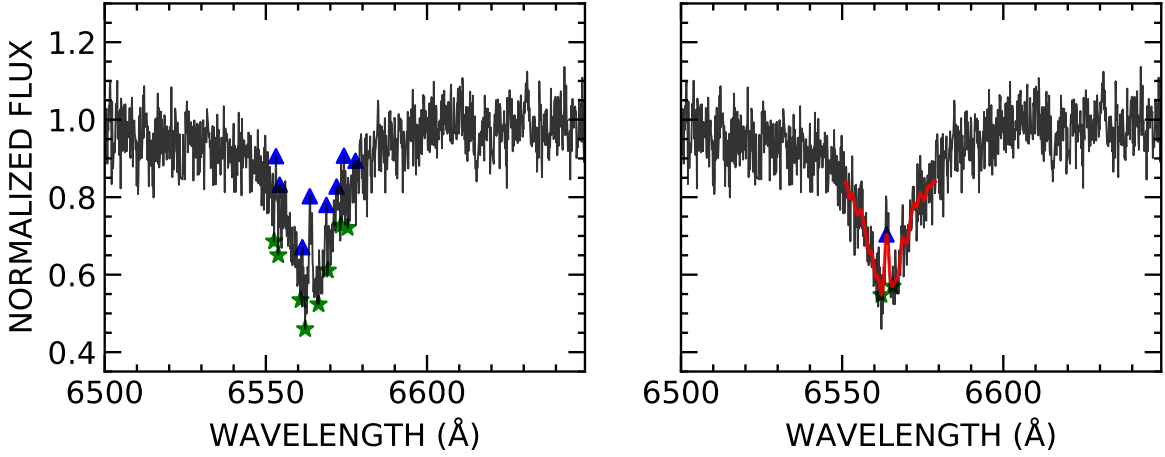
#### 4.1.1. Identifying H $\alpha$ peak featured spectra

In order to apply the **ResNet** to identify the Be spectra in the MRS database, we first need to construct the training sample. Both Be spectra, and non-Be spectra should be included to represent a broad range of spectral features in the sample. Because H $\alpha$  emission profiles feature the optical spectra of CBe stars, thus we are expected to obtain negative *EW* values measured over the profile. However, in those cases of weak emission, as shown in [Figure 3](#), the H $\alpha$  peak is superimposed on the bottom of a broad absorption feature. The dominant absorption feature leads to positive calculated values of *EW*, and such stars will be missed from the selection using a simple criterion of positive *EW* value.

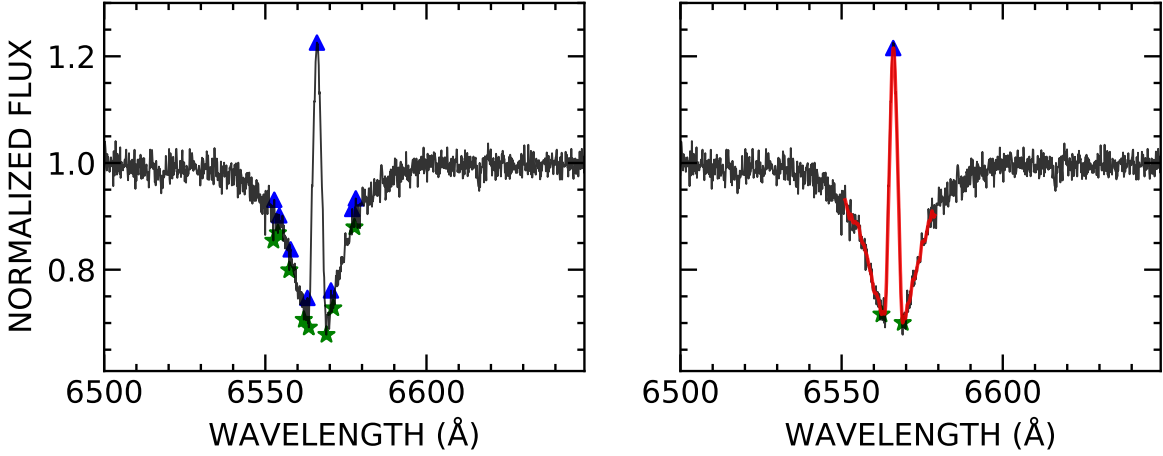
In order to confirm the detection of the H $\alpha$  peak feature in the sample spectra, we restricted the profile within a wavelength region of 6551 – 6579 Å to search for the peak pixels with local maximum flux values. In [Figure 3](#), we show two example spectra of stars J023209.36+560939.5 and J071536.32–001018.3, observed in the red band from the LAMOST MRS in panels (a) and (b), respectively. As shown in the left panels of (a) and (b), multiple locations of the valley pixels (green star) and the peak pixels (blue triangle) were determined from the line profile. To avoid the ambiguity of locating the global maximum pixels from the local peak pixels, we adopted a Bartlett window approach from [Bartlett \(1950\)](#) to smooth the spectra over the selected wavelength region. In the top right panel of [Figure 3](#), we experimented with various window sizes to smooth the selected portion of the H $\alpha$  profile for J023209.36+560939.5 to identify the peak feature, and 15 pixels were chosen for this spectrum with S/N = 13. The smooth spectra over the selected region are shown in the red line and are over-plotted on top of the observed spectra shown in black. Due to the higher S/N for the spectrum of J071536.32–001018.3 (S/N = 50), we selected a smaller window size of 9 pixels to perform the smoothing process (bottom right panel of [Figure 3](#)). In [Table 1](#), we list the S/N ranges and selected widths of the Bartlett window function for spectra in our sample.

<sup>3</sup> <https://pytorch.org/vision/stable/models.html>





(a) J023209.36+560939.5



(b) J071536.32-001018.3

**Figure 3.** The spectra of stars J023209.36+560939.5 (panel a) and J071536.32-001018.3 (panel b) were observed in the red band from the LAMOST MRS. *Left panels:* Multiple locations of the valley pixels (blue star) and peak pixels (blue triangle) were determined from the  $H\alpha$  profile over the wavelength region of 6551–6579 Å. *Right panels:* By adopting a Bartlett window smoothing approach from Bartlett (1950), the location of the peak pixels with local maximum flux values is determined. Based on the S/N of the spectra, a window size of 15 pixels was chosen to smooth the profile over selected wavelength regions for J023209.36+560939.5, and the smoothed spectra are shown in red-line and over-plotted on the observed spectrum shown in black (top right panel). A window size of 9 pixels was selected in the case of J071536.32-001018.3 (bottom right panel).

#### 4.1.2. Constructing the training sample for the ResNet

**Table 1.** Selected width of the Bartlett window function

S/N	Window width
Range	(pixel)
$10 \leq S/N < 20$	15
$20 \leq S/N < 40$	10
$40 \leq S/N < 60$	9
$60 \leq S/N < 100$	8
$100 \leq S/N < 120$	7
$120 \leq S/N < 150$	6
$S/N \geq 150$	5

We visually inspected the spectra with identified H $\alpha$  features as discussed in Section 4.1.1 and found 1,042 spectra as the Be candidate spectra for the training sample. A broad representation of the morphological features for the Be candidate spectra is selected. In Figure 4, we show example Be spectra displaying emission profiles, including both single peaked H $\alpha$  profile (panel a) and double emission peaks (panel b); those cases of weak emission profiles that are superimposed on the bottom of a broad absorption feature (panels c and d); and also absorption shell line profiles (panels e and f). In Table 2, we list the LAMOST designation ID, the equatorial coordinates, the observational date, and the S/N for the found 1,042 Be candidate star. Since the training sample should include spectral features for both Be and non-Be spectra and maintain a symmetric number of observations for each category, we also visually selected 1,042 non-Be spectra from the sample of 257,860 early-type stellar spectra as discussed in Section 3 to include any non-emission features in the training sample. Example spectra for the non-Be stars, such as strong H $\alpha$  absorption profiles (top panel) and weak featured spectra (bottom panel), are shown in Figure 5. In Table 3, we list the selected non-Be spectra in the same format as Table 2.

We solely utilized the spectra observed in the red band of LAMOST MRS to perform the Be star identification task using the ResNet algorithm. The final training sample consists of 1,042 spectra of Be candidate stars and 1,042 spectral of non-Be stars. We generated their spectral images in a short wavelength range of 6530 – 6590 Å and maintained the same size of 256 × 256 pixels for each spectral image. We divided the sample into a training set comprising 80% of the spectral images and a validation set containing 20% of the spectral images.

#### 4.1.3. Data augmentation

The network achieves a higher performance of identifying input data if both the training errors and validation errors show a decreasing trend towards an increasing training time applied to the module (see Figure 1 of Shorten & Khoshgoftaar 2019). This can be achieved using a very powerful technique

**Table 2.** Be candidate spectra selected for the training sample

LAMOST spectrum ID	RA (deg)	DEC (deg)	Date (MJD)	S/N
611012036	0.0161	63.9082	58089.8069	63
596908120	0.0878	55.4570	58057.9354	228
595809135	0.1068	62.6628	58055.8813	49
611109135	0.1068	62.6628	58089.8514	70
596908134	0.1744	55.7225	58057.9354	145
611012151	0.3529	63.5044	58089.8069	159
609212029	0.6556	58.4759	58087.7910	145
596906238	0.9008	55.8183	58057.9354	129
611006213	1.1282	61.2467	58089.8278	54
611106196	1.1745	61.4988	58089.8514	69

NOTE—This table is available in its entirety in machine-readable form. The first ten entries are shown here for guidance regarding its format and content.

**Table 3.** non-Be candidate spectra selected for the training sample

LAMOST spectrum ID	RA (deg)	DEC (deg)	Date (MJD)	S/N
608405246	13.0407	59.1671	58085.8076	76
684203235	13.4165	37.2534	58419.9174	98
611804047	13.4377	60.4097	58090.8479	82
608405084	13.5333	58.7219	58085.8076	103
611805039	13.7602	59.0381	58090.8479	84
608404219	14.3077	60.5316	58085.8076	110
608404118	14.5391	59.8807	58085.8076	105
611809107	15.0439	61.1058	58090.8479	71
684208174	15.6540	37.0037	58419.9174	102
611808033	15.6748	59.8273	58090.8479	69

NOTE—This table is available in its entirety in machine-readable form. The first ten entries are shown here for guidance regarding its format and content.

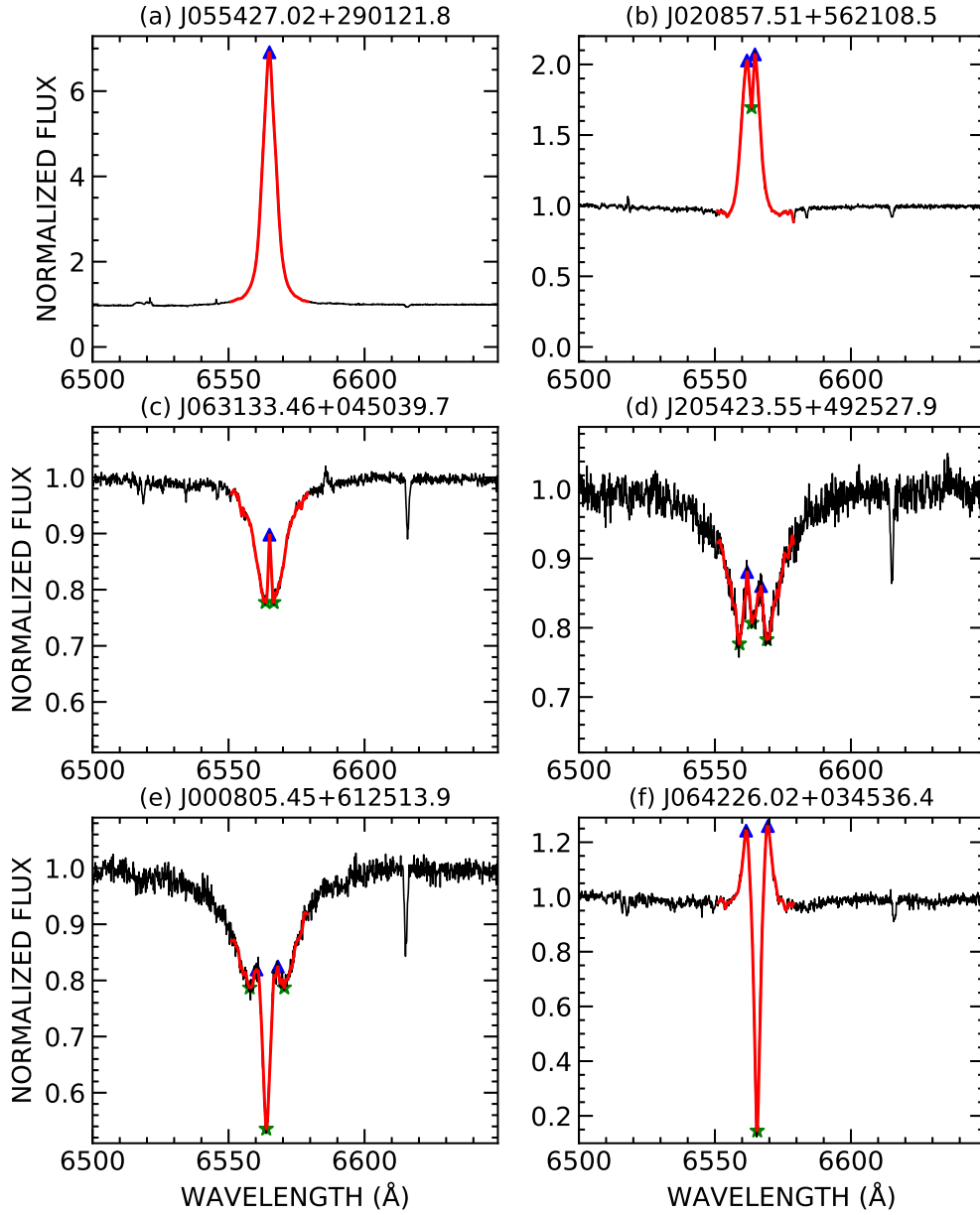
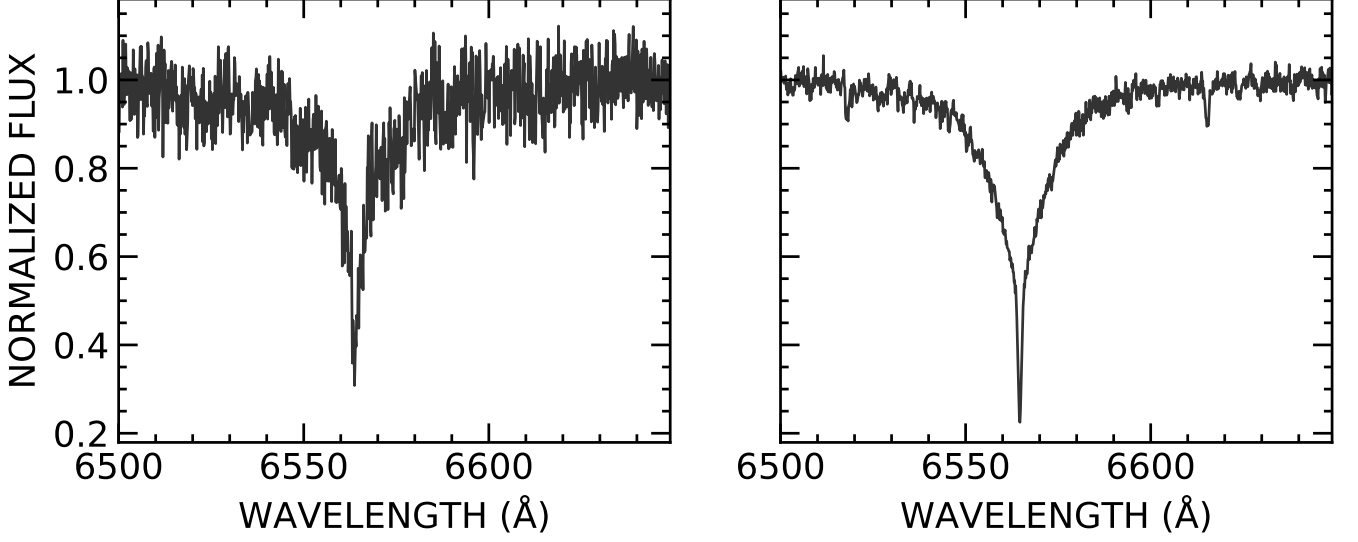
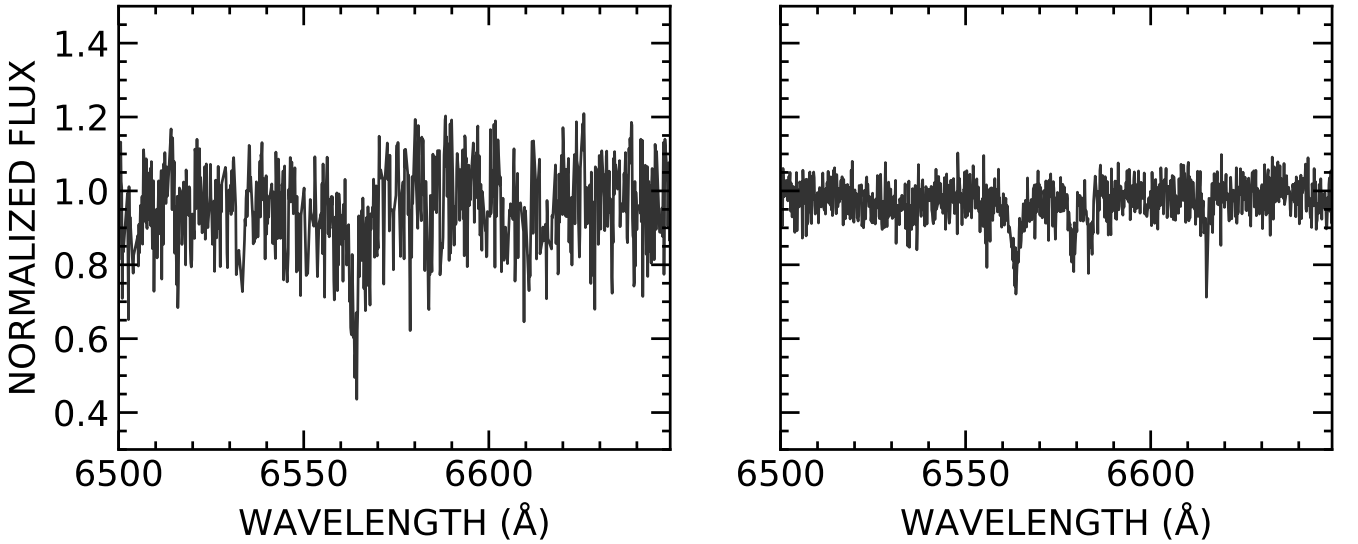


**Figure 4.** A broad representation of the morphological features for the Be candidate spectra is selected for the training sample of **ResNet**. The spectra included examples of single-peaked (panel a) and double-peaked emission profiles (panel b); emission profiles superimposed on the bottom of broad absorption profiles (panels c and d); and shell line profiles (panels e and f). The valley pixels, peak pixels, and the smoothed portion of the profile are labeled on the plot in each panel in the same format as Figure 3.

known as data augmentation, which is the standard procedure for training models in computer vision



(a) J000357.80+564258.4 (left) and J010743.93+585138.9 (right)



(b) J000222.70+625403.1 (left) and J004953.72+643816.5 (right)

**Figure 5.** Example spectra for non-Be stars with  $H\alpha$  absorption profiles randomly selected from the sample of 257,860 as discussed in Section 3.

tasks. Such a process expands the dataset by generating different versions of the data with some transformations. Instead of simply increasing the number of samples, data augmentation can improve the performance of the model since it is a regularisation method that reduces the structural risk of the model and helps to avoid over-fitting (Mikołajczyk & Grochowski 2018).

We thus applied a series of geometric transformations to augment the diversity of the training set such that a broad representation of  $H\alpha$  profile variations is included, and meanwhile, to preserve the morphological features of  $H\alpha$  profiles. In this data augmentation process, the following techniques

were applied to the spectra images: rotating the images slightly at random in the range of  $-10^\circ$  to  $+10^\circ$ , zooming the images with multiples between 1.0 and 1.5, warping images in perspective, and flipping the images along the vertical axis. Data augmentation allows the network to learn these invariants in the dataset. It does not change the sample distribution and main characteristics of the data but creates variability and increases the diversity (Wong et al. 2016; Shorten & Khoshgoftaar 2019). As a result, the robustness and generalization ability of the model can be improved.

#### 4.1.4. Applying the ResNet

By applying the **ResNet** to our training sample, the model learns a broad representation of  $H\alpha$  features. We used accuracy as the performance metric to evaluate the quality of the model. The accuracy is defined as the ratio of the number of correct samples to the number of total samples. In Figure 6, we show the result of the identification task performed by the learning module for input spectra from the validation set after training the **ResNet** for ten epochs. Among the set, 209 images with the pre-labeled spectral feature of Be stars were identified as True Positive (TP) detections (shown in the upper left panel of Figure 6), while 205 pre-labeled non-Be featured images were classified as True Negative (TN) by the **ResNet** (lower right panel). None of the predicted non-Be spectral featured images were identified as a positive detection by the classifier, denoted as False Negative (FN), suggesting that all the Be star spectra features were recognized by the classifier (shown in the upper right panel of Figure 6). Such findings indicate that our model achieves an accuracy of 99.5%, and most of the sample spectra can be classified well by the module. However, two images with predicted labels of Be spectral features were labeled as non-Be type stars from the learning module (lower left panel of Figure 6), indicating that the identified Be star sample may include a small fraction of spurious detection due to the misclassification (denoted as False Positive, FP). We thus visually inspected the sample of identified Be candidate stars obtained from the **ResNet** and arrived with a preliminary sample of 1,134 Be candidate stars.

#### 4.2. The morphological classification of the $H\alpha$ emission stars

Based upon the morphological features of the  $H\alpha$  profile shown in the red spectra of the Be candidate stars identified from the usage of **ResNet**, we visually inspected the spectra of the stars and grouped them into two categories of emission lines and shell line features. Among the sample of 1,134 Be candidate stars, 822 stars display  $H\alpha$  emission profiles in their spectra, 113 stars show absorption shell line features superimposed on top of the broad  $H\alpha$  emission profiles, and 199 stars display shell line features superimposed on top of the absorption  $H\alpha$  profile. In Figure 7, we show examples of profiles with single  $H\alpha$  emission (panel a), symmetric double emission peaks (panel b), asymmetric double emission peaks (panel c), and a narrow emission superimposed on top of an absorption profile (panel d). We also classified the  $H\alpha$  shell line featured stars into subgroups based upon their shell line width and symmetry, and the complete catalogs listing the morphological classification of these spectra are discussed in the Appendix.

### 5. IDENTIFICATION OF CLASSICAL Be STARS FROM THE PRELIMINARY SAMPLE

#### 5.1. Literature cross-matching

Following the selection of the preliminary sample of Be stars reported in Section 4, we applied a three-step test to the selected stars to identify the CBe stars. We first adopted the primary defining criterion of the CBe stars, the presence of the Balmer emission line feature in the spectra to visually



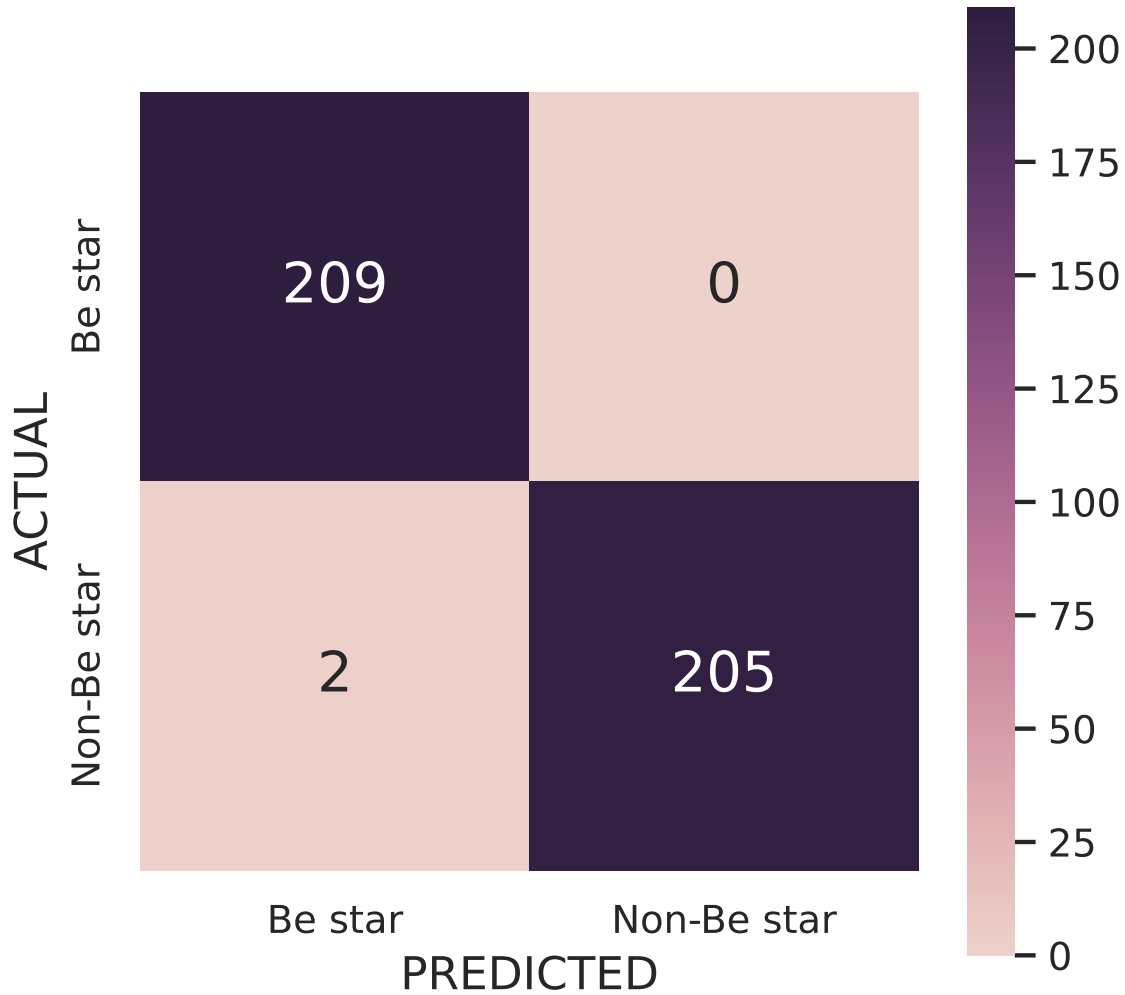


**Figure 6.** Representation for the performance of the `ResNet` applied to the  $H\alpha$  featured spectra in the validation set. The upper left panel shows the TP detection of the learning module, and 209 spectra in the validation set with predicted Be spectra features were identified as the true label. The lower right panel shows the TN detection for 205 pre-labeled non-Be stars. The upper right panel shows the null detection of any pre-label non-Be stars identified as a Be star in the set, suggesting that none of the Be star spectral features were missed from the learning model. The lower left panel shows the spurious detection of Be stars due to misclassification. The `ResNet` model achieves an accuracy of 99.5%.

select stars displaying  $H\alpha$  emission using spectra observed from the LAMOST MRS red arm. This criterion resulted in a collection of 822 stars identified in the sample of 1,134 Be candidate stars. We then performed a literature search to cross-match stars in the sample with prior classified CBe stars. The major resources include the catalog of 1,159 Be stars by [Jaschek & Egret \(1982\)](#); the BeSS database ([Neiner et al. 2011](#)), a total collection of 2,195 CBe stars as of 2021 April 13; 213 Be stars from the APOGEE survey by [Chojnowski et al. \(2015\)](#); detections of 192 CBe candidate stars from the LAMOST DR1 Low-Resolution Survey (LRS) from [Lin et al. \(2015\)](#); a comprehensive compilation of 1,991 sources from the BeSS, APOGEE, and the INT Photometric  $H\alpha$  Survey of the Northern Galactic Plane (IPHAS) from [Chen et al. \(2016\)](#); the Be catalog of 5,603 stars identified from the LAMOST DR2 database from [Hou et al. \(2016\)](#); the 693 newly classified CBe candidate

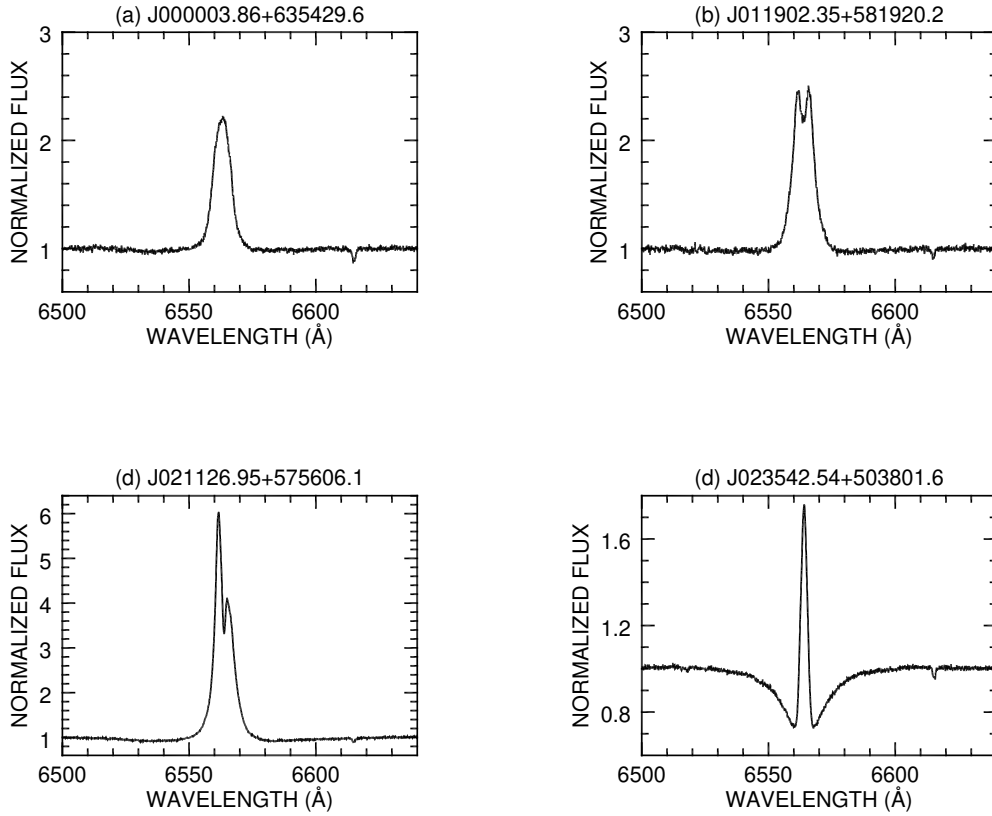


**Figure 7.** The  $H\alpha$  emission profiles of stars selected from the LAMOST MRS DR7 database with various morphological features. (a) J000003.86+635429.6 with a single emission peak, (b) J011902.35+581920.2 with symmetric double emission peaks, (c) J021126.95+575606.1, and (d) J023542.54+503801.6 with a narrow emission peak superimposed on top of an absorption profile.

stars found using *Gaia* DR2 observations by Vioque et al. (2020); and the 2,716 hot emission-line identified using the LAMOST DR5 LRS by Shridharan et al. (2021). We also cross-matched stars in our sample with those discussed in publications to search for any known Herbig Ae/Be stars, and 12 such stars were found from the literature searches. Some of the target stars may display  $H\alpha$  emission being contaminated by ionized nebulae in H II regions. Three stars in the sample were found from the cross-matching of known stars in Hou et al. (2016), who listed a collection of 3,600 contaminated emission stars. The emission lines of  $H\alpha$ , [N II]  $\lambda$ 6548,  $\lambda$ 6583, He I  $\lambda$ 6678, and [S II]  $\lambda$ 6717,  $\lambda$ 6731 are shown in the red spectra, and [O III]  $\lambda$ 4959,  $\lambda$ 5007 feature is shown in the blue spectra of these stars. The number of stars found from the literature search appears in Table 4. After removing duplications, a total collection of 151 CBe stars are found from the literature search, resulting in the preliminary sample narrowed to 671 new CBe candidate stars. We show the LAMOST designation ID, right ascension (RA), declination (DEC), star name, spectral classification, and the associated reference of the cross-matched known CBe stars in Table 6.

**Table 4.** Common stars found from literature cross-matching

Object type	Number of stars found	Reference
CBe stars	43	Neiner et al. (2011)
CBe stars	10	Chojnowski et al. (2015)
CBe stars	3	Lin et al. (2015)
CBe stars	9	Chen et al. (2016)
CBe stars	63	Hou et al. (2016)
CBe stars	36	Vioque et al. (2020)
Herbig Ae/Be stars	3	Herbst & Shevchenko (1999)
Herbig Ae/Be stars	1	Vieira et al. (2003)
Herbig Ae/Be stars	2	Neiner et al. (2011)
Herbig Ae/Be stars	1	Hou et al. (2016)
Herbig Ae/Be stars	5	Vioque et al. (2020)
HII regions	3	Hou et al. (2016)

### 5.2. Spectral type collection

We then cross-matched the stars with the spectral classification catalogs of Skiff (2014) and Kharchenko & Roeser (2009) to collect their spectral types. We complement the search with the usage of SIMBAD (Wenger et al. 2000) for stars not found in these catalogs. In the case of stars with contradicting spectral types, we adopted the classification from the most recent available publication. We conservatively excluded stars from the sample with no record of spectral type. Among the H $\alpha$  emission stars with archived spectral types from literature, we identified eight O-type emission line stars from the sample and listed their LAMOST designations, star names, equatorial coordinates, spectral types, and the associated references in Table 5. Stars with spectral types later than O8 and earlier than A2-type only were selected as potential CBe candidate stars, and we also excluded stars with the luminosity class of I and II appearing in their spectral classification. A collection of 222 stars were cross-matched from the catalogs that satisfy this second test.

### 5.3. The IR test

We caution that the candidate CBe stars in the sample may be contaminated by the presence of pre-main-sequence Herbig Ae/Be stars, which also display H $\alpha$  emission profiles. The similarity of their H $\alpha$  emission features often confuses the classification of the CBe stars. Finkenzeller & Mundt (1984) suggested that the Herbig Ae/Be stars display stronger IR excess compared to CBe stars, and the two types of stars can be distinguished from the IR photometry through position in a ( $H - K$ ,  $K - L$ ) color-color diagram. Hou et al. (2016) demonstrated the applicability of replacing the  $L$  band with the *WISE*  $W_1$  band to separate the two classes in a ( $H - K$ ,  $K - W_1$ ) color-color diagram. We thus adopt this approach to identify the CBe stars in our preliminary sample. We cross-matched stars in our sample with those in the *AllWISE* Data Release from Cutri et al. (2021), and 206 stars

**Table 5.** Oe stars found from the LAMOST MRS DR7 sample

LAMOST designation	Star Name	RA (deg)	DEC (deg)	Spectral Classification	Spectral Classification Reference
J000441.87+612955.7	EM VES 682	1.1745	61.4988	O9 III	3
J000925.08+624718.2	EM GGR 172	2.3545	62.7884	O9	4
J040320.74+511852.5	BD+50 886	60.8365	51.3146	O4 V((c))	85
J052000.64+385443.4	LS V +38 12	80.0027	38.9121	O6.5 V((f))	85
J202937.57+405108.5	UCAC4 655-091969	307.4066	40.8524	O8 III((f))	85
J203457.84+414354.2	RLP 1252	308.7410	41.7317	O8 Ve	85
J222830.98+560054.7	EM AS 491	337.1291	56.0152	O5	4
J234528.61+631616.7	LS I +62 14	356.3692	63.2713	O5: Iafpe	85

NOTE—Indices of references: (3) [Martin \(1972\)](#) (4) [Reed \(2003\)](#) (85) [Li \(2021\)](#). This table is available in machine-readable form.

were found with recorded measurements in the  $J$ ,  $H$ ,  $K$ , and  $W_1$  bands. Because of the presence of interstellar dust, extinction corrections were applied to the archived photometric measurements. We obtained the reddening values of the stars from the empirical three-dimensional dust map from [Green et al. \(2019\)](#) based upon their equatorial coordinates and distance. The latter quantity was collected from the *Gaia* EDR3 ([Bailer-Jones et al. 2021](#)). We adopted the extinction ratio  $A_\lambda/A_V$  values listed in Table 3 of [Cardelli et al. \(1989\)](#), which are based upon a ratio of total to selective extinction of  $R_V = A_V/E(B - V) = 3.1$  ([Fitzpatrick 1999](#)). The adopted ratios have values of 0.282, 0.190, and 0.114 for the  $J$ ,  $H$ ,  $K$  filters, respectively. We then adopted the extinction coefficient for the *WISE*  $W_1$  band from [Yuan et al. \(2013\)](#) with  $A_{W_1}/A_V = 0.061$ . According to the selecting criterion given by [Hou et al. \(2016\)](#), Herbig Ae/Be stars are founded in the range of  $H - K > 0.4$  and  $K - W_1 > 0.8$  in the color-color magnitude diagram, while the CBe stars have  $H - K < 0.2$  and  $K - W_1 < 0.5$ . We applied these criteria to the corrected photometric measurements to identify CBe and Herbig Ae/Be stars. This leads to a total identification of 183 new CBe stars and two Herbig Ae/Be stars. In Table 7, we list the LAMOST designation ID, star name, right ascension (RA), declination (DEC), spectral classification, reference of the classification, the *AllWISE* photometric measurements of  $J$ ,  $H$ ,  $K$ ,  $W_1$  bands, their associated errors, and the reddening for each new detection.

Based on literature cross-matching and new identifications, a total collection of 334 CBe stars are found from the LAMOST MRS DR7 database. In Figure 8, we show the distribution with the number of observations of the entire sample (solid line) and the 183 new detections (line filled) of all the CBe stars in the left panel. One hundred ninety-five of the CBe stars were observed in a single visit. The right panel displays the number distribution of the CBe stars versus the observational baseline.

## 6. OPEN CLUSTER MEMBERSHIP AND KINEMATICS OF THE CBe STARS

**Table 6.** Known Be stars found from the LAMOST MRS DR7 sample

LAMOST designation	Star Name	RA (deg)	DEC (deg)	Spectral Classification	Spectral Classification Reference
J000124.69+633015.7	BD+62 2346	0.3529	63.5044	B0 V	3
J000145.61+632758.0	...	0.4401	63.4661	B	1
J010642.79+615941.9	...	16.6783	61.9950	...	...
J011833.07+582230.5	HD 236689	19.6378	58.3751	B1.5 Vep_sh	10
J011854.11+581206.8	BD+57 243	19.7255	58.2019	B3	66
J012319.41+573851.7	BD+56 259	20.8309	57.6477	B3e	33
J012401.03+585036.1	VES 704	21.0043	58.8434	Be	67
J012429.14+601723.2	BD+59 246	21.1214	60.2898	Ae	68
J012718.47+600653.6	BD+59 250	21.8270	60.1149	B0e	19
J012924.35+590557.3	BD+58 247	22.3515	59.0993	B1/2e	69

NOTE—Indices of references: (1) Brodskaya (1955) (3) Martin (1972) (10) Morgan et al. (1955) (19) Merrill et al. (1942) (33) Merrill & Burwell (1949) (66) Hayford (1932) (67) Miller & Merrill (1951) (68) Merrill & Burwell (1950) (69) McCuskey et al. (1974). This table is available in its entirety in machine-readable form. The first ten entries are shown here for guidance regarding its format and content.

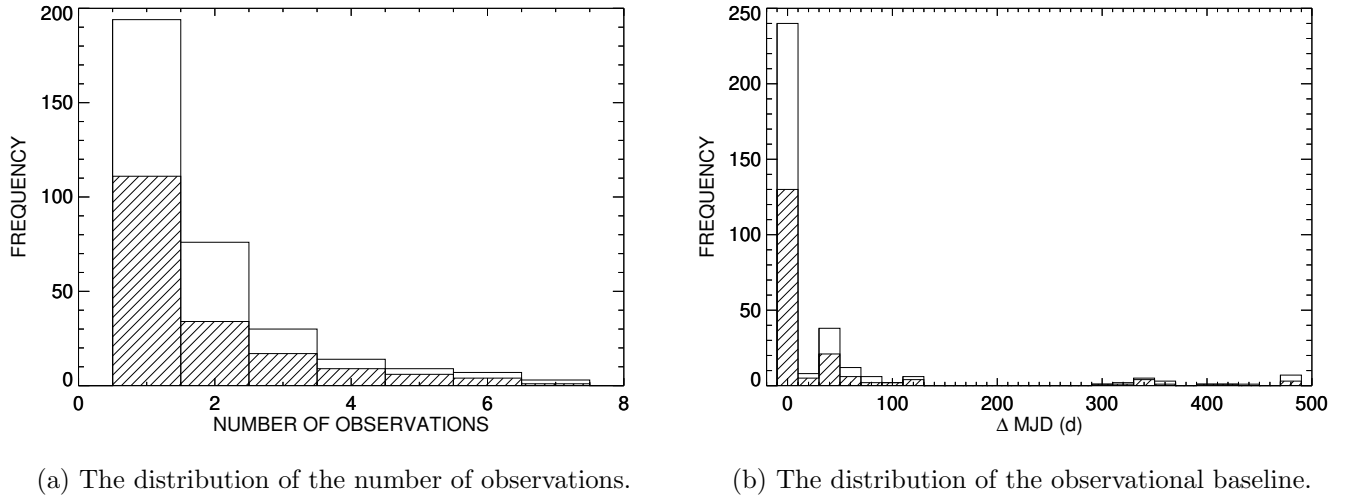


**Figure 8.** The left panel plots the distribution of the number of observations for the full sample of 334 CBe stars found from the LAMOST MRS DR7 database, and the right panel plots the distribution of the observational baseline ( $\Delta \text{MJD} = \text{MJD}_{max} - \text{MJD}_{min}$ ) of the sample stars. The full sample is shown in solid line, and the new 183 detections are shown with filled lines.

**Table 7.** Newly identified CBe stars from the LAMOST MRS DR7 sample

LAMOST designation	Star Name	RA (deg)	DEC (deg)	Spectral Classification	Reference	$J$ (mag)	$\sigma_J$ (mag)	$H$ (mag)	$\sigma_H$ (mag)	$K$ (mag)	$\sigma_K$ (mag)	$W_1$ (mag)	$\sigma_{W_1}$ (mag)	$E(B - V)$ (mag)
J000035.31+623317.7	TYC 4018-3553-1	0.1472	62.5549	B2	1	11.030	0.021	10.944	0.030	10.921	0.023	10.591	0.023	0.320
J000430.77+611448.2	EM* VES 681	1.1282	61.2467	B2	2	9.484	0.022	9.274	0.028	9.063	0.022	9.082	0.022	0.560
J000441.87+612955.7	EM* VES 682	1.1745	61.4988	O9 III	3	10.667	0.024	10.527	0.031	10.448	0.030	10.426	0.022	0.392
J000925.08+624718.2	EM* GGR 172	2.3545	62.7884	O9	4	10.092	0.018	9.857	0.017	9.632	0.022	9.274	0.023	0.436
J001324.32+591313.4	LS I +58 13	3.3514	59.2204	OBe	5	9.407	0.020	9.196	0.020	9.022	0.022	9.132	0.023	0.816
J001930.74+600218.4	LS I +59 39	4.8781	60.0385	OB	5	9.592	0.022	9.390	0.032	9.187	0.022	9.054	0.023	0.570
J002459.27+591931.4	EM* GGR 183	6.2470	59.3254	A	14	11.371	0.028	11.157	0.033	10.955	0.028	10.645	0.023	0.581
J002629.20+600127.9	LS I +59 42	6.6217	60.0244	OBe	5	10.048	0.027	9.715	0.032	9.430	0.024	9.638	0.024	0.820
J002935.50+601817.8	EM* GGR 187	7.3979	60.3049	Ae	6	10.796	0.019	10.708	0.027	10.662	0.025	10.624	0.023	0.450
J004315.45+595219.9	EM* GGR 201	10.8144	59.8722	Ae	6	10.748	0.019	10.527	0.028	10.289	0.023	10.017	0.022	0.520

NOTE—Indices of references: (1) Brodskaya (1955) (2) Brodskaya (1953) (3) Martin (1972) (4) Reed (2003) (5) Hardorp et al. (1959) (6) González & González (1956) (14) Wenger et al. (2000). This table is available in its entirety in machine-readable form. The first ten entries are shown here for guidance regarding its format and content.



We are interested in determining the potential membership of the identified 334 CBe stars in the known open clusters (OC). We examined the OC data from the work of [Cantat-Gaudin et al. \(2018\)](#), who compiled the star members and cluster parameters for 1,229 OCs using *Gaia* DR2 astrometric data; a compilation of 226 OCs using the data from *Gaia* DR2, GALAH+, and APOGEE DR16 from [Spina et al. \(2021\)](#); and a comprehensive collection of fundamental parameters, including the mean radial velocity ( $V_r$ ), distance, age, metallicity, and extinction for 1,743 OCs from [Dias et al. \(2021\)](#). We collected the equatorial coordinates ( $RA$  and  $DEC$ ), the proper motion ( $\mu_\alpha$  and  $\mu_\beta$ ), the parallax ( $\pi$ ), and the associated uncertainty parameters for each of the CBe stars from the *Gaia* EDR3 ([Gaia Collaboration et al. 2016, 2021](#)) using a circular search aperture of  $1''$ . A quality filter of the Renormalised Unit Weight Error (RUWE)  $> 1.4$  was applied to omit any problematic astrometric measurements.

We first cross-matched the equatorial coordinates and proper motions of the CBe stars with member stars with a classified membership probability  $> 60\%$  of the known OCs. Because stars may be located either in the foreground or the background of the OC, we then cross-matched the parallaxes of CBe stars with those measurements of cluster member stars. We identified 41 CBe stars that are associated with known OCs, and report their LAMOST designation and cluster name in the first two columns of Table 8, respectively. Fundamental parameters of cluster radial velocity  $V_r$ , derived distance, cluster age, metallicity, extinction, and their associated errors taken from the compilation from [Dias et al. \(2021\)](#) are listed in columns 3 to 12. Among these identified cluster member stars, 13 of them are located in the same cluster of NGC 884 ( $\chi$  Persei), [Marsh Boyer et al. \(2012\)](#) conducted a spectroscopic investigation including 46 Be stars in this cluster to determine their physical properties and reported that they are likely more evolved than stars found in similar open clusters.

The OB runaway stars are stars with high spatial velocities that may travel far from the Galactic plane. [Blaauw \(1961\)](#) suggested that the origin of OB runaway stars may be a result of binary supernovae scenario, in which the massive primary star of the binary system evolved to a supernova and the lower mass secondary companion was released to become a high-velocity runaway star. Alternatively, [Poveda et al. \(1967\)](#) proposed that the runaway stars may originate from a dynamic ejection mechanism as a consequence of gravitational interaction between stars in clusters. The origins and ejection mechanism for such runaways can be traced from studying the kinematics of the stars. Based upon the newly identified CBe stars from this work, by utilizing the astrometric solutions provided by the *Gaia* EDR3, we are interested in investigating the kinematic properties of the CBe stars by measuring the peculiar tangential velocities and searching for any possible runaway candidates. In order to measure the peculiar component velocities of the sample stars, we collected the available astrometric solutions for 323 CBe stars from the *Gaia* EDR3 and applied the quality filter following the same way as described in Section 6. We first transformed the equatorial coordinates of the sample stars to the Galactic coordinate systems by adopting the coordinate of the north Galactic pole of  $(\alpha_G, \delta_G) = (192.95948^\circ, 27.12825^\circ)$  at the epoch of J2000.0 from the Hipparcos consortium. We then performed the matrix transformations for peculiar motions of the sample stars following the equations listed in [Moffat et al. \(1998, 1999\)](#). In order to subtract the contributions of the solar motion and the differential Galactic rotation from the peculiar motion of the CBe stars, we adopted the Solar motion of  $(U_\odot, V_\odot, W_\odot) = (11.10, 12.24, 7.25)$  km s $^{-1}$  from [Schönrich et al. \(2010\)](#). A flat rotation curve from [Kerr & Lynden-Bell \(1986\)](#) is adopted with the Solar galactocentric distance

with value of  $R_0 = 8.5$  kpc and the circular Galactic rotational velocity of  $V_c = 220$  km s<sup>-1</sup>. We plot the distribution of the peculiar tangential velocities for the CBe sample in Figure 9.

Stars with observed space velocities greater than 40 km s<sup>-1</sup> are classified as runaway stars (Blaauw 1961). Many following works have adopted similar runaway criteria to search for runaway stars in the Galaxy either through measurements of the peculiar space motions or through the individual peculiar velocity components (radial or tangential components), such as using the Hipparcos astrometric observations to identify Galactic OB runaways (Gies & Bolton 1986; Mdzinarishvili & Chargeishvili 2005; Tetzlaff et al. 2011), field O-type stars, and Wolf-Rayet stars (Gies 1987; Moffat et al. 1998; de Wit et al. 2005). Berger & Gies (2001) utilized the Hipparcos measurements to identify runaway Be stars by adopting a selection criterion of peculiar space velocity greater than 40 km s<sup>-1</sup>. Due to the absence of radial velocity measurements for the identified CBe stars in our sample, instead of adopting the historical runaway velocity limit, we thus rely on the peculiar tangential velocity to identify any potential runaway candidates. Because the distribution of peculiar tangential velocity includes contributions from both the longitudinal and latitudinal directions, a simple Gaussian is insufficient to describe such distribution. Hobbs et al. (2005) investigated the proper motion for a sample of pulsars and reported that a Maxwellian velocity distribution is well fitted to the space velocities of the stars. We then fitted a Maxwellian velocity distribution (Equation 1) to the peculiar tangential velocities,

$$f(v) = av^2 \exp(-v^2/b^2) \quad (1)$$

where  $a = 0.904 \pm 0.029$  and  $b = 8.701 \pm 0.094$  km s<sup>-1</sup>, and the distribution was overplotted in Figure 9. We defined the criterion of runaway stars in our sample to stars with the peculiar tangential velocities greater than the value at  $\sim 1\%$  of the peak distribution from the Maxwellian fit, and this corresponds to a runaway velocity limit of  $V_{Tp} > 24$  km s<sup>-1</sup>. Based upon this proposed criterion for identifying the runaway stars, we identified 16 Be runaways from the sample of 323 stars. In Table 9, we report the queried proper motions and parallax from the *Gaia* EDR3, measured peculiar tangential velocities ( $V_{Tp}$ ), and the associated uncertainties for the identified runaway candidate stars in columns 2 to 9. We also include the estimated heights of the runaway stars from the Galactic plane in the last column of Table 9 adopting  $z = r \sin b + z_\odot$ , where  $z_\odot$  with a value of 20.5 pc is taken from Humphreys & Larsen (1995).

We report a runaway rate of  $\sim 5\%$  for identified CBe stars from the LAMOST MRS DR7 sample, and this detection rate is comparable to the results reported by Berger & Gies (2001), who suggests a runaway frequency of 3  $\sim$  7% based upon an investigation of peculiar space motions for a sample of 344 Be stars. However, our result is significantly lower than the finding of  $\sim 13.1\%$  from Boubert & Evans (2018), in which a comprehensive collection of 632 Be stars were collected to investigate the runaway population of Be stars through a Bayesian approach. We caution that the runaway fraction from the prior studies is based on measured peculiar space motion in both radial and tangential components. We may have missed the detections of runaways in our sample due to the absence of radial velocity measurements. We cross-matched the stars listed in Table 9 to known runaways published in the literature, and no common stars are found, thus suggesting that these runaways are new identifications.

Based upon the photometric observations for the CBe stars obtained from *Gaia*, we show the location of both the newly identifications and literature cross-matched CBe stars on a  $G_{BP} - G_{RP}$  VS  $M_G$  color-magnitude diagram. We collected the photometric flux measurements from  $G_{BP}$ ,  $G_{RP}$ ,

and  $G$  bands from *Gaia* EDR3. As suggested by *Gaia* Collaboration et al. (2018), the flux excess factor (with a flag of `phot_bp_rp_excess_factor`) within a range of  $1.0 + 0.015 \times (G_{BP} - G_{RP})^2 \leq E \leq 1.3 + 0.06 \times (G_{BP} - G_{RP})^2$  was checked for each observation to reject any excess flux recorded in the  $G_{BP}$  and  $G_{RP}$  bands. We further adopted the approach from Luri et al. (2018) to convert the observed apparent  $G$  magnitude to absolute  $M_G$  magnitude (see their Equation 22). In Figure 10, we show the  $G_{BP} - G_{RP}$  VS  $M_G$  color-magnitude plot for 179 new identifications (blue) and literature cross-matched 149 CBe stars (black) with available measurements from *Gaia*. The CBe stars are located on the color-magnitude diagram as expected for Be stars.

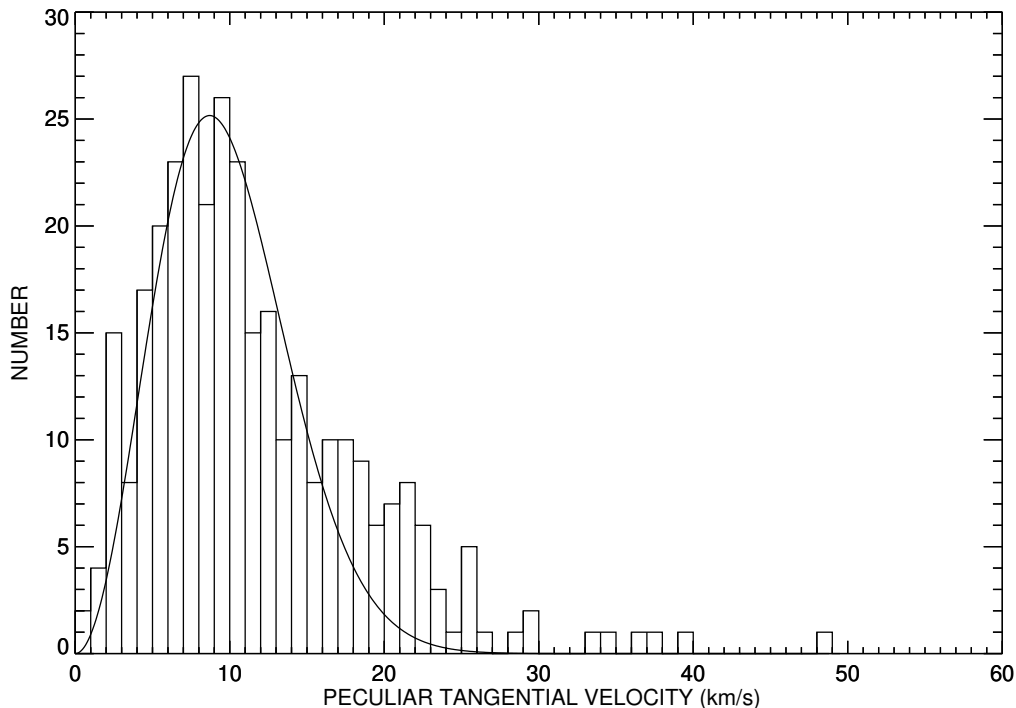


**Figure 9.** The distribution of peculiar tangential velocities for 323 CBe stars identified from the LAMOST MRS DR7. A Maxwellian velocity distribution was fitted to the peculiar tangential velocities.

## 7. SUMMARY AND CONCLUSIONS

The classical Be stars are B-type main-sequence stars surrounded by circumstellar disks that create Balmer emission lines in their spectra. Here we examined the large and homogenous spectroscopic observations in the LAMOST MRS DR7 survey, we use a deep convolutional neural network, *ResNet* to identify CBe stars from their  $H\alpha$  properties.

Table 8. Open cluster memberships for identified CBe stars from the LAMOST MRS DR7 sample

LAMOST designation	Cluster Name	Cluster $V_r$ (km s $^{-1}$ )	$\sigma(V_r)$ (km s $^{-1}$ )	Distance (pc)	$\sigma(d)$ (pc)	$\log Age$ (yr)	$\sigma(Age)$ (yr)	$[Fe/H]$	$\sigma([Fe/H])$	$A_V$ (mag)	$\sigma(A_V)$ (mag)
J011524.01+583108.5	NGC 457	-4.6	1.1	2540	133	7.373	0.073	-0.034	0.153	1.612	0.020
J011540.89+584902.1	NGC 436	-79.8	0.4	2743	118	7.861	0.105	-0.122	0.110	1.590	0.034
J011604.49+584651.2	NGC 436	-79.8	0.4	2743	118	7.861	0.105	-0.122	0.110	1.590	0.034
J011833.06+582230.4	NGC 457	-4.6	1.1	2540	133	7.373	0.073	-0.034	0.153	1.612	0.020
J011854.11+581206.8	NGC 457	-4.6	1.1	2540	133	7.373	0.073	-0.034	0.153	1.612	0.020
J011902.35+581920.2	NGC 457	-4.6	1.1	2540	133	7.373	0.073	-0.034	0.153	1.612	0.020
J014430.77+584610.9	COIN-Gaia 4	...	...	1853	146	8.238	0.318	-0.104	0.103	1.767	0.134
J015822.85+552725.9	NGC 744	...	...	1258	40	8.261	0.249	0.019	0.076	1.116	0.107
J021346.59+600208.3	COIN-Gaia 35	...	...	2354	290	7.013	0.616	-0.140	0.174	2.726	0.091
J021547.53+572514.2	UBC 46	...	...	2003	77	7.613	0.140	-0.143	0.072	1.762	0.033
J022142.93+570530.6	NGC 884	...	...	2150	103	7.187	0.050	-0.079	0.092	1.709	0.019
J022143.39+570732.8	NGC 884	...	...	2150	103	7.187	0.050	-0.079	0.092	1.709	0.019
J022144.47+571052.2	NGC 884	...	...	2150	103	7.187	0.050	-0.079	0.092	1.709	0.019
J022145.96+570500.9	NGC 884	...	...	2150	103	7.187	0.050	-0.079	0.092	1.709	0.019
J022202.47+570920.4	NGC 884	...	...	2150	103	7.187	0.050	-0.079	0.092	1.709	0.019
J022204.56+571038.8	NGC 884	...	...	2150	103	7.187	0.050	-0.079	0.092	1.709	0.019
J022246.97+565805.8	NGC 884	...	...	2150	103	7.187	0.050	-0.079	0.092	1.709	0.019
J022248.96+570913.9	NGC 884	...	...	2150	103	7.187	0.050	-0.079	0.092	1.709	0.019
J022250.28+570850.6	NGC 884	...	...	2150	103	7.187	0.050	-0.079	0.092	1.709	0.019
J022304.18+570738.7	NGC 884	...	...	2150	103	7.187	0.050	-0.079	0.092	1.709	0.019
J022324.92+571903.3	NGC 884	...	...	2150	103	7.187	0.050	-0.079	0.092	1.709	0.019
J022328.16+572325.6	NGC 884	...	...	2150	103	7.187	0.050	-0.079	0.092	1.709	0.019
J022432.59+570044.8	NGC 884	...	...	2150	103	7.187	0.050	-0.079	0.092	1.709	0.019
J022650.54+572020.1	UBC 192	...	...	2239	75	7.278	0.176	0.021	0.072	1.773	0.036
J023005.94+571833.8	UBC 606	...	...	2463	54	7.000	0.236	-0.127	0.133	2.168	0.036
J023058.70+571503.8	UBC 192	...	...	2239	75	7.278	0.176	0.021	0.072	1.773	0.036
J050317.28+234917.4	NGC 1750	-9.7	1.1	707	7	8.296	0.196	0.060	0.057	1.239	0.034
J053607.20+340803.2	NGC 1960	...	...	1086	37	7.480	0.059	-0.030	0.085	0.929	0.024
J054946.16+285952.8	Czemik 23	14.3	0.5	3102	221	8.495	0.617	-0.132	0.167	1.743	0.155
J060452.44+240331.3	IC 2157	...	...	1885	155	7.552	0.185	-0.098	0.055	1.651	0.051
J061410.98+123607.0	NGC 2194	41.6	1.4	2869	83	8.823	0.050	-0.067	0.066	1.562	0.075
J062140.49+265806.2	Gulliver 56	...	...	1943	51	8.350	0.174	-0.100	0.047	0.968	0.076
J063131.81+053051.6	NGC 2244	92.3	1.2	1254	89	7.111	0.090	-0.214	0.084	1.571	0.063
J063337.49+044847.0	NGC 2244	92.3	1.2	1254	89	7.111	0.090	-0.214	0.084	1.571	0.063
J063701.44+051307.0	Collinder 107	...	...	1466	85	7.183	0.129	-0.100	0.163	1.465	0.071
J184244.50-060913.6	UBC 104	...	...	2741	151	8.428	0.634	0.295	0.112	1.781	0.154
J185103.91-061732.0	NGC 6705	35.7	0.2	1888	65	8.469	0.085	0.043	0.063	1.457	0.051
J221255.97+572639.0	NGC 7235	...	...	3158	261	7.100	0.117	0.018	0.115	2.566	0.031
J221950.08+572428.5	LP 1809	-84.3	3.1	2707	191	8.644	0.645	0.092	0.116	2.729	0.191
J221951.45+580853.4	NGC 7261	...	...	2389	106	7.632	0.088	0.010	0.096	2.731	0.029
J235039.51+605439.1	FSR 0451	...	...	2602	120	7.077	0.024	-0.095	0.063	2.291	0.045

NOTE—This table is available in its entirety in machine-readable form.

**Table 9.** The peculiar velocities of the 16 runaway CBe stars identified from the LAMOST MRS DR7 sample

LAMOST	$\mu_\alpha$	$\sigma$	$\mu_\beta$	$\sigma$	Parallax	$\sigma$	$V_{Tp}$	$\sigma$	$z$
designation	(mas yr <sup>-1</sup> )	(mas yr <sup>-1</sup> )	(mas yr <sup>-1</sup> )	(mas yr <sup>-1</sup> )	(mas)	(mas)	(km s <sup>-1</sup> )	(km s <sup>-1</sup> )	(pc)
J032822.23+450756.0	2.4793	0.0240	-0.0143	0.0194	0.3898	0.0209	34.3	1.9	212.6
J041706.17+490757.2	0.7924	0.0172	-2.3405	0.0145	0.3515	0.0172	24.7	1.2	31.5
J044532.80+441554.7	4.1211	0.0231	-6.8914	0.0172	0.7670	0.0174	36.7	0.9	44.8
J044800.93+401847.9	0.1580	0.0193	-0.8861	0.0149	0.1140	0.0150	26.2	3.6	82.6
J055812.33+274333.7	-0.8517	0.0247	0.5285	0.0173	0.3135	0.0208	25.0	1.7	94.8
J060421.79+283840.7	0.8418	0.0245	-2.7897	0.0174	0.3663	0.0223	25.1	1.6	62.1
J061358.64+124327.3	-0.2615	0.0162	-3.2853	0.0130	0.4242	0.0157	29.8	1.1	41.6
J062945.80+173216.5	0.8607	0.0339	-2.4530	0.0259	0.3150	0.0292	33.4	3.2	170.0
J185103.91-061732.0	-1.5166	0.0236	-4.1254	0.0193	0.3748	0.0264	25.9	1.9	100.5
J221950.08+572428.5	-3.6236	0.0149	-2.8681	0.0142	0.2148	0.0134	29.1	1.9	154.4
J221951.45+580853.4	-3.8237	0.0119	-3.1010	0.0123	0.2858	0.0115	25.4	1.1	192.2
J222236.47+531945.9	-4.5890	0.0188	-3.7029	0.0173	0.2318	0.0149	48.8	3.2	123.3
J222426.67+573834.4	-3.8290	0.0134	-3.7036	0.0116	0.3252	0.0119	28.4	1.1	177.2
J223529.46+564759.7	-3.7224	0.0148	-3.0935	0.0138	0.2040	0.0139	39.4	2.7	161.1
J234525.42+564015.2	-1.5749	0.0150	0.9009	0.0153	0.4647	0.0160	25.3	0.9	62.4
J235756.00+625549.6	-4.2501	0.0137	-1.1622	0.0144	0.2653	0.0136	37.7	2.0	295.8

NOTE—This table is available in its entirety in machine-readable form.

Our first task was to form an initial sample of early-type stars (with the spectral classification of O-type to early A-type only) from a collection of 2,260,387 spectra for 789,918 stars from the database. We rejected 1,973,886 spectra for late A-type and F-type stars from the sample using the estimated  $T_{\text{eff}}$  values as given from the *LASP*. Through calculations of the equivalent widths of H $\alpha$   $\lambda$ 6563 and Mg I  $b$  triplet line profiles, by forming a distribution of  $EW$  over the two selected line indices, we excluded any hidden late-type stars and narrowed the sample down to 261,647 spectra. Further filtering of K-type and M-type stars was achieved by inspecting their locations on a color-color diagram using the IR photometric observations from the *2MASS* all-sky survey. We selected a collection of 257,860 early-type stellar spectra from the MRS DR7 database.

In order to apply the **ResNet** network to identify Be candidate stars from the initial sample of 257,860 early-type stellar spectra, we first adopted a Bartlett window smoothing approach to smooth observed spectra over a wavelength region of 6551 – 6579 Å to identify the H $\alpha$  peak features in the sample. Through visual inspection, we constructed a training sample of 2,084 spectra, in which 1,042 of them were found as Be candidate spectra showing H $\alpha$  peak feature in their profiles, and the rest of the spectra were randomly chosen from the initial sample as non-Be spectra. By applying the **ResNet-18** learning module and then confirming the identification with a visual inspection, we arrived at a preliminary list of 1,162 Be stars identified from the DR7 database. The learning module achieved a classification accuracy of 99.5%.

We cross-matched these candidate stars with published catalogs and found that 151 of them are known CBe stars. By further applying a three-step test, 183 new detections were identified from the sample. Based upon cross-matching the equatorial coordinates, proper motion, and parallax of the identified CBe stars with those of known open clusters, we identified 41 cluster member stars. The parent clusters of these member stars have ages between 10~655 Myr, with metallicity  $[Fe/H]$  spans a range of -0.214~0.295. We also explored the kinematics of the identified CBe stars by measuring their peculiar tangential velocities based upon astrometric solutions from the *Gaia* EDR3 and identified

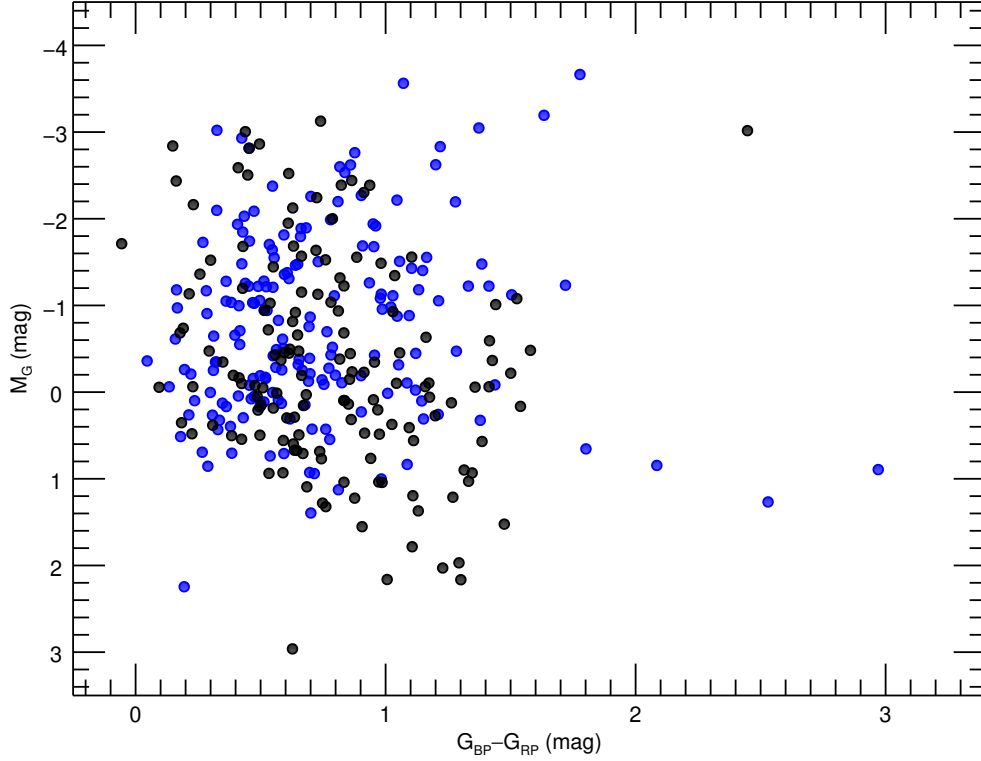


**Figure 10.** The  $G_{BP} - B_{RP}$  VS  $G_G$  color-magnitude diagram for CBe stars identified from the LAMOST MRS DR7 database. The newly identified CBe stars from this work are plotted in blue and the prior known CBe stars cross-matched from literature are in black.

16 new runaways from the sample. These newly identified runaways correspond to a  $\sim 5\%$  detection rate, which is comparable to the findings reported from earlier studies made from the *Hipparcos* observations. These runaways have measured Galactic heights between  $30\sim 300$  pc from the Galactic disc, no high-latitude CBe stars were found in the sample. Both the dynamic ejection mechanism and the binary supernova scenario suggest that the formation of runaways is associated with binary systems. Leonard & Duncan (1990) performed an N-body simulation for the former scenario and estimated a binary fraction of 10% for runaways. In contrast, a binary frequency of  $30\sim 40\%$  was reported from Portegies Zwart (2000) by utilizing binary population synthesis calculations for the binary supernova scenario. Future investigation for the binary properties of these newly identified runaways from the LAMOST MRS sample will be helpful to constrain their formation channel.

In this work, we have demonstrated the applicability of applying the neural network **ResNet** to identify the spectral features of CBe stars from a large collection of observations efficiently and accurately. We have built the Be spectra classifier using the **ResNet** module for the observations from the LAMOST MRS DR7 through the identification of  $H\alpha$  peak featured spectra and the construction of the training sample. In our future work, we plan to include the spectral processing process into the classifying scheme, such as the spectral rectification, and release the code as a public accessible



package. By providing input spectra obtained from the database, such a classifier will automatically rectify the spectra and perform the classification task to further improve the identification efficiency. Because of the limited wavelength coverage of the MRS spectra, we solely relied on the spectra recorded in the red arm covering the  $H\alpha$  profile to perform the identification task. We are optimized about the future work of applying this technique to the low-resolution spectra (LRS) from the LAMOST database since such spectra display a broader optical wavelength coverage to include the major atmospheric line profiles of Be stars compared to the MRS spectra. The extensive collection of spectroscopic observations made from the LAMOST MRS DR7 database comprises the first of the five-year time-domain observing campaign, with the future spectra from the forthcoming DR8 and DR9, we would expect to enlarge the current sample size of CBe stars. This information will provide a reference for future investigations of the Be population and its physical and evolutionary properties.

1 This work was supported by the Chinese National Science Foundation under programs of No.  
 2 12090040, 12090043, 11733008, and 12103064. Guoshoujing Telescope (the Large Sky Area Multi-  
 3 Object Fiber Spectroscopic Telescope LAMOST) is a National Major Scientific Project built by the  
 4 Chinese Academy of Sciences. Funding for the project has been provided by the National Development  
 5 and Reform Commission. LAMOST is operated and managed by the National Astronomical Obser-  
 6 vatories, Chinese Academy of Sciences. This work has made use of data from the European Space  
 7 Agency (ESA) mission *Gaia* (<https://www.cosmos.esa.int/gaia>), processed by the *Gaia* Data Pro-  
 8 cessing and Analysis Consortium (DPAC, <https://www.cosmos.esa.int/web/gaia/dpac/consortium>).  
 9 Funding for the DPAC has been provided by national institutions, in particular the institutions  
 10 participating in the *Gaia* Multilateral Agreement. This work has made use of the BeSS database,  
 11 operated at LESIA, Observatoire de Meudon, France: <http://basebe.obspm.fr>.

*Facilities:* LAMOST, Gaia

## APPENDIX

### A. MORPHOLOGICAL CLASSIFICATION OF THE $H\alpha$ SHELL LINE SPECTRA

Shell line features appear in the  $H\alpha$  profile of 312 Be candidate stars. The red spectra of 113 Be candidate stars display a superimposed absorption shell line on top of the  $H\alpha$  emission profile. We classified these emission shell line profiles into three sub-categories: a spectrum with symmetric narrow absorption shell profile denoted as Type 1, a spectrum with symmetric broad absorption shell profile (Type 2), and an asymmetric absorption shell (Type 3). In Figure A1, we show the example spectra of Type 1 and Type 2 in panels (a) to (b), respectively. An asymmetric absorption shell line superimposed on top of the  $H\alpha$  emission profile of Type 3 spectra is shown in panels (c) and (d). We report the LAMOST designation ID, right ascension (RA), declination (DEC) in the first three columns of Table A1, and list the shell line type for each of the stars in the last column of the table.

Shell line features were superimposed on top of a broad  $H\alpha$  absorption profile for the rest of the 199 shell stars. In Figure A2, we show examples of shell line spectra with an emission component above the spectral continuum (Type 1, panel a), an emission component below the spectral continuum

(Type 2, panel b), and a narrow absorption shell line (Type 3, panel c). We classified these stars into sub-types based upon the shell line classification as mentioned through visual inspection. The equatorial coordinates and the classification types are collected in Table A2, in the same format as Table A1.

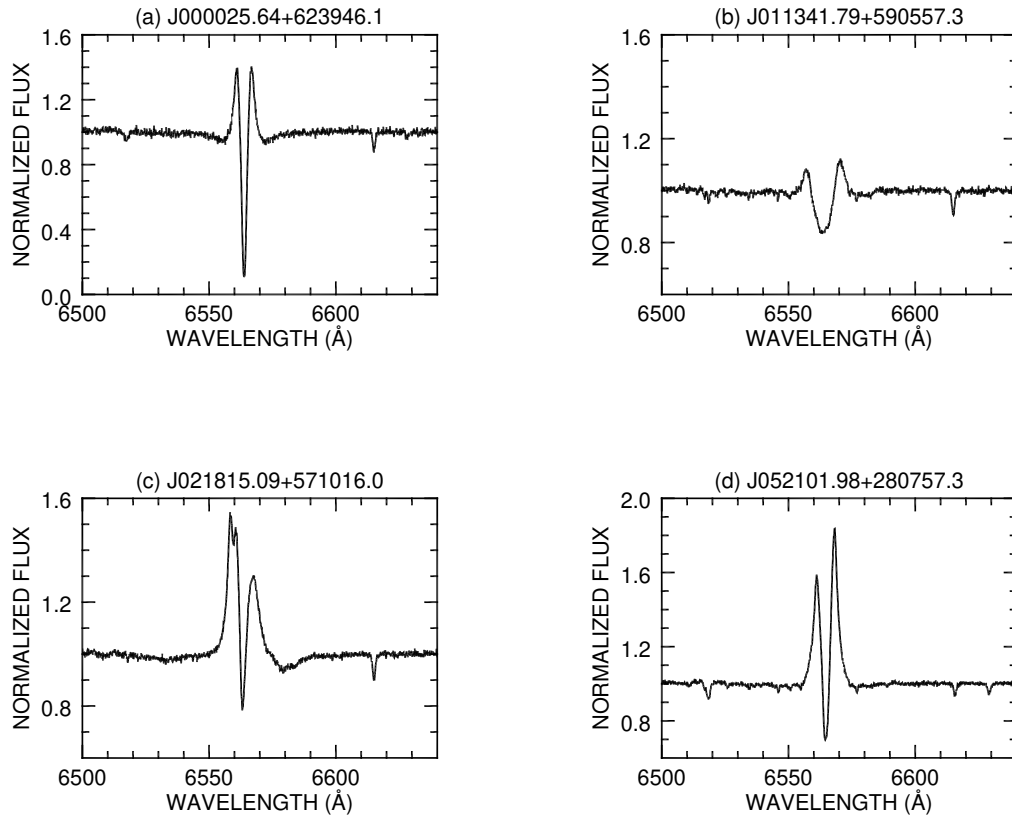


**Figure A1.** The H $\alpha$  emission profiles superimposed with an absorption shell line identified from the LAMOST MRS DR7 database. (a) J000025.64+623946.1 (Type 1), (b) J011341.79+590557.3 (Type 2), (c) J021815.09+571016.0 (Type 3), and (d) J052101.98+280757.3 (Type 3).

## REFERENCES

- Aidelman, Y., Escudero, C., Ronchetti, F., Quiroga, F., & Lanzarini, L. 2020, Communications in Computer and Information Science book series, 1291, 111, doi: [10.1007/978-3-030-61218-4\\_8](https://doi.org/10.1007/978-3-030-61218-4_8)
- Allen-Zhu, Z., & Li, Y. 2019, arXiv e-prints, arXiv:1905.10337. <https://arxiv.org/abs/1905.10337>

**Table A1.** Candidate Be stars displaying  $H\alpha$  emission profiles with absorption shell line identified from the LAMOST MRS DR7 sample

LAMOST designation	RA (deg)	DEC (deg)	Type Index
J000025.64+623946.1	0.1068	62.6628	1
J000336.20+554905.9	0.9008	55.8183	3
J000719.05+615350.5	1.8294	61.8974	1
J004746.45+601122.5	11.9436	60.1896	1
J011341.79+590557.3	18.4241	59.0993	2
J011507.07+581812.5	18.7795	58.3035	3
J011623.65+590507.3	19.0986	59.0854	1
J011623.65+590507.4	19.0986	59.0854	1
J012318.25+580435.1	20.8261	58.0764	3
J013131.58+594607.5	22.8816	59.7688	2

NOTE—This table is available in its entirety in machine-readable form. The first ten entries are shown here for guidance regarding its format and content.

**Table A2.** Candidate Be stars displaying  $H\alpha$  absorption profiles with shell line identified from the LAMOST MRS DR7 sample

LAMOST designation	RA (deg)	DEC (deg)	Type Index
J000021.08+552725.1	0.0878	55.4570	2
J000056.27+625702.5	0.2345	62.9507	2
J000237.33+582833.3	0.6556	58.4759	2
J000452.79+623619.8	1.2200	62.6055	1
J000805.45+612513.9	2.0227	61.4205	3
J002922.13+580036.7	7.3422	58.0102	3
J003150.41+573524.4	7.9601	57.5901	2
J003504.28+604317.5	8.7678	60.7216	2
J011242.62+595723.1	18.1776	59.9564	1
J011249.59+593434.2	18.2066	59.5762	1

NOTE—This table is available in its entirety in machine-readable form. The first ten entries are shown here for guidance regarding its format and content.

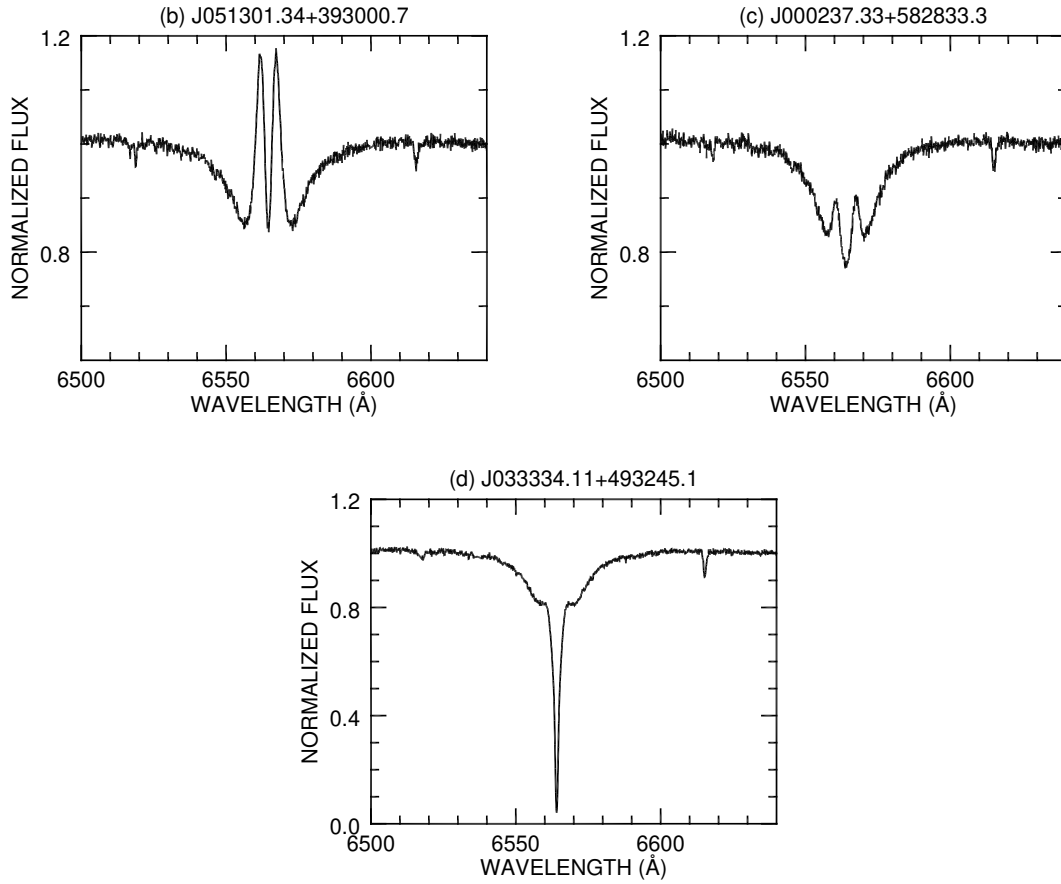


**Figure A2.** The  $H\alpha$  absorption profiles superimposed with a shell line identified from the LAMOST MRS DR7 database. (a) J051301.34+393000.7 (Type 1), (b) J000237.33+582833.3 (Type 2), and (c) J033334.11+493245.1 (Type 3).

- Arora, S., Du, S. S., Hu, W., et al. 2019, arXiv e-prints, arXiv:1904.11955.  
<https://arxiv.org/abs/1904.11955>
- Bailer-Jones, C. A. L., Rybizki, J., Fouesneau, M., Demleitner, M., & Andrae, R. 2021, *VizieR Online Data Catalog*, I/352
- Bartlett, M. S. 1950, *Biometrika*, 37, 1.  
<http://www.jstor.org/stable/2332141>
- Berger, D. H., & Gies, D. R. 2001, *ApJ*, 555, 364,  
 doi: [10.1086/321461](https://doi.org/10.1086/321461)
- Blaauw, A. 1961, *BAN*, 15, 265
- Boubert, D., & Evans, N. W. 2018, *MNRAS*, 477, 5261, doi: [10.1093/mnras/sty980](https://doi.org/10.1093/mnras/sty980)
- Brodskaya, E. S. 1953, *Izvestiya Ordena Trudovogo Krasnogo Znameni Krymskoj Astrofizicheskoj Observatorii*, 10, 104
- . 1955, *Izvestiya Ordena Trudovogo Krasnogo Znameni Krymskoj Astrofizicheskoj Observatorii*, 14, 3
- Brown, J. C., Telfer, D., Li, Q., et al. 2004, *MNRAS*, 352, 1061,  
 doi: [10.1111/j.1365-2966.2004.07997.x](https://doi.org/10.1111/j.1365-2966.2004.07997.x)
- Cantat-Gaudin, T., Jordi, C., Vallenari, A., et al. 2018, *A&A*, 618, A93,  
 doi: [10.1051/0004-6361/201833476](https://doi.org/10.1051/0004-6361/201833476)
- Cardelli, J. A., Clayton, G. C., & Mathis, J. S. 1989, *ApJ*, 345, 245, doi: [10.1086/167900](https://doi.org/10.1086/167900)
- Casares, J., Negueruela, I., Ribó, M., et al. 2014, *Nature*, 505, 378, doi: [10.1038/nature12916](https://doi.org/10.1038/nature12916)
- Chen, P. S., Liu, J. Y., & Shan, H. G. 2016, *MNRAS*, 463, 1162,  
 doi: [10.1093/mnras/stw1757](https://doi.org/10.1093/mnras/stw1757)
- Chojnowski, S. D., Whelan, D. G., Wisniewski, J. P., et al. 2015, *AJ*, 149, 7,  
 doi: [10.1088/0004-6256/149/1/7](https://doi.org/10.1088/0004-6256/149/1/7)
- Cohen, J. G., Blakeslee, J. P., & Ryzhov, A. 1998, *ApJ*, 496, 808, doi: [10.1086/305429](https://doi.org/10.1086/305429)
- Comerón, F., & Pasquali, A. 2005, *A&A*, 430, 541,  
 doi: [10.1051/0004-6361:20041788](https://doi.org/10.1051/0004-6361:20041788)
- Comerón, F., Pasquali, A., Rodighiero, G., et al. 2002, *A&A*, 389, 874,  
 doi: [10.1051/0004-6361:20020648](https://doi.org/10.1051/0004-6361:20020648)
- Cutri, R. M., Skrutskie, M. F., van Dyk, S., et al. 2003, *VizieR Online Data Catalog*, II/246
- Cutri, R. M., Wright, E. L., Conrow, T., et al. 2021, *VizieR Online Data Catalog*, II/328
- de Wit, W. J., Testi, L., Palla, F., & Zinnecker, H. 2005, *A&A*, 437, 247,  
 doi: [10.1051/0004-6361:20042489](https://doi.org/10.1051/0004-6361:20042489)
- Deng, J., Dong, W., Socher, R., et al. 2009, in 2009 IEEE Conference on Computer Vision and Pattern Recognition, 248–255,  
 doi: [10.1109/CVPR.2009.5206848](https://doi.org/10.1109/CVPR.2009.5206848)
- Dias, W. S., Monteiro, H., Moitinho, A., et al. 2021, *MNRAS*, 504, 356,  
 doi: [10.1093/mnras/stab770](https://doi.org/10.1093/mnras/stab770)
- Finkenzeller, U., & Mundt, R. 1984, *A&AS*, 55, 109
- Fitzpatrick, E. L. 1999, *PASP*, 111, 63,  
 doi: [10.1086/316293](https://doi.org/10.1086/316293)
- Gaia Collaboration, Prusti, T., de Bruijne, J. H. J., et al. 2016, *A&A*, 595, A1,  
 doi: [10.1051/0004-6361/201629272](https://doi.org/10.1051/0004-6361/201629272)
- Gaia Collaboration, Brown, A. G. A., Vallenari, A., et al. 2018, *A&A*, 616, A1,  
 doi: [10.1051/0004-6361/201833051](https://doi.org/10.1051/0004-6361/201833051)
- . 2021, *A&A*, 649, A1,  
 doi: [10.1051/0004-6361/202039657](https://doi.org/10.1051/0004-6361/202039657)
- Ghoreyshi, M. R., Carciofi, A. C., Jones, C. E., et al. 2021, *ApJ*, 909, 149,  
 doi: [10.3847/1538-4357/abdd1e](https://doi.org/10.3847/1538-4357/abdd1e)
- Gies, D. R. 1987, *ApJS*, 64, 545,  
 doi: [10.1086/191208](https://doi.org/10.1086/191208)
- Gies, D. R., & Bolton, C. T. 1986, *ApJS*, 61, 419,  
 doi: [10.1086/191118](https://doi.org/10.1086/191118)
- Gkouvelis, L., Fabregat, J., Zorec, J., et al. 2016, *A&A*, 591, A140,  
 doi: [10.1051/0004-6361/201527090](https://doi.org/10.1051/0004-6361/201527090)
- González, G., & González, G. 1956, *Boletín de los Observatorios Tonantzintla y Tacubaya*, 2, 16
- Gray, R. O., & Corbally, Christopher, J. 2009, *Stellar Spectral Classification* (Princeton University Press)
- Green, G. M., Schlafly, E., Zucker, C., Speagle, J. S., & Finkbeiner, D. 2019, *ApJ*, 887, 93,  
 doi: [10.3847/1538-4357/ab5362](https://doi.org/10.3847/1538-4357/ab5362)
- Guo, Y., Li, J., Xiong, J., et al. 2021, arXiv e-prints, arXiv:2109.09775.  
<https://arxiv.org/abs/2109.09775>
- Hardorp, J., Rohlfs, K., Slettebak, A., & Stock, J. 1959, *Hamburger Sternw. Warner & Swasey Obs.*, C01, 0
- Hayford, P. 1932, *Lick Observatory Bulletin*, 448, 53, doi: [10.5479/ADS/bib/1932LicOB.16.53H](https://doi.org/10.5479/ADS/bib/1932LicOB.16.53H)
- He, K., Zhang, X., Ren, S., & Sun, J. 2016a, in *Computer Vision – ECCV 2016*, ed. B. Leibe, J. Matas, N. Sebe, & M. Welling (Cham: Springer International Publishing), 630–645

- He, K., Zhang, X., Ren, S., & Sun, J. 2016b, in Proceedings of the IEEE Conference on Computer Vision and Pattern Recognition (CVPR)
- Herbst, W., & Shevchenko, V. S. 1999, VizieR Online Data Catalog, J/AJ/118/1043
- Hobbs, G., Lorimer, D. R., Lyne, A. G., & Kramer, M. 2005, MNRAS, 360, 974, doi: [10.1111/j.1365-2966.2005.09087.x](https://doi.org/10.1111/j.1365-2966.2005.09087.x)
- Hou, W., Luo, A. L., Hu, J.-Y., et al. 2016, Research in Astronomy and Astrophysics, 16, 138, doi: [10.1088/1674-4527/16/9/138](https://doi.org/10.1088/1674-4527/16/9/138)
- Hubrig, S., Briquet, M., Schöller, M., et al. 2006, MNRAS, 369, L61, doi: [10.1111/j.1745-3933.2006.00175.x](https://doi.org/10.1111/j.1745-3933.2006.00175.x)
- Hubrig, S., Schöller, M., Savanov, I., et al. 2009, Astronomische Nachrichten, 330, 708, doi: [10.1002/asna.200911236](https://doi.org/10.1002/asna.200911236)
- Humphreys, R. M., & Larsen, J. A. 1995, AJ, 110, 2183, doi: [10.1086/117677](https://doi.org/10.1086/117677)
- Jaschek, M., & Egret, D. 1982, in Be Stars, ed. M. Jaschek & H. G. Groth, Vol. 98, 261
- Kerr, F. J., & Lynden-Bell, D. 1986, MNRAS, 221, 1023, doi: [10.1093/mnras/221.4.1023](https://doi.org/10.1093/mnras/221.4.1023)
- Kharchenko, N. V., & Roeser, S. 2009, VizieR Online Data Catalog, I/280B
- Kingma, D. P., & Ba, J. 2014, arXiv e-prints, arXiv:1412.6980. <https://arxiv.org/abs/1412.6980>
- Klement, R., Carciofi, A. C., Rivinius, T., et al. 2019, ApJ, 885, 147, doi: [10.3847/1538-4357/ab48e7](https://doi.org/10.3847/1538-4357/ab48e7)
- Lecun, Y., Bengio, Y., & Hinton, G. 2015, Nature, 521, 436, doi: [10.1038/nature14539](https://doi.org/10.1038/nature14539)
- Lee, U., Osaki, Y., & Saio, H. 1991, MNRAS, 250, 432, doi: [10.1093/mnras/250.2.432](https://doi.org/10.1093/mnras/250.2.432)
- Leonard, P. J. T., & Duncan, M. J. 1990, AJ, 99, 608, doi: [10.1086/115354](https://doi.org/10.1086/115354)
- Li, G.-W. 2021, ApJS, 253, 54, doi: [10.3847/1538-4365/abe716](https://doi.org/10.3847/1538-4365/abe716)
- Li, R., Shu, Y., Su, J., et al. 2019, MNRAS, 482, 313, doi: [10.1093/mnras/sty2708](https://doi.org/10.1093/mnras/sty2708)
- Lin, C.-C., Hou, J.-L., Chen, L., et al. 2015, Research in Astronomy and Astrophysics, 15, 1325, doi: [10.1088/1674-4527/15/8/015](https://doi.org/10.1088/1674-4527/15/8/015)
- Liu, C., Fu, J., Shi, J., et al. 2020, arXiv e-prints, arXiv:2005.07210. <https://arxiv.org/abs/2005.07210>
- Luo, A. L., Zhao, Y.-H., Zhao, G., et al. 2015, Research in Astronomy and Astrophysics, 15, 1095, doi: [10.1088/1674-4527/15/8/002](https://doi.org/10.1088/1674-4527/15/8/002)
- Luri, X., Brown, A. G. A., Sarro, L. M., et al. 2018, A&A, 616, A9, doi: [10.1051/0004-6361/201832964](https://doi.org/10.1051/0004-6361/201832964)
- Maheswaran, M. 2003, ApJ, 592, 1156, doi: [10.1086/375797](https://doi.org/10.1086/375797)
- Marsh Boyer, A. N., McSwain, M. V., Aragona, C., & Ou-Yang, B. 2012, AJ, 144, 158, doi: [10.1088/0004-6256/144/6/158](https://doi.org/10.1088/0004-6256/144/6/158)
- Martin, N. 1972, A&A, 17, 253
- McCuskey, S. W., Pesch, P., & Snyder, G. A. 1974, AJ, 79, 597, doi: [10.1086/111581](https://doi.org/10.1086/111581)
- Mdzinarishvili, T. G., & Chargeishvili, K. B. 2005, A&A, 431, L1, doi: [10.1051/0004-6361:200400134](https://doi.org/10.1051/0004-6361:200400134)
- Merrill, P. W., & Burwell, C. G. 1949, ApJ, 110, 387, doi: [10.1086/145215](https://doi.org/10.1086/145215)
- . 1950, ApJ, 112, 72, doi: [10.1086/145319](https://doi.org/10.1086/145319)
- Merrill, P. W., Burwell, C. G., & Miller, W. C. 1942, ApJ, 96, 15, doi: [10.1086/144428](https://doi.org/10.1086/144428)
- Mikołajczyk, A., & Grochowski, M. 2018, in 2018 International Interdisciplinary PhD Workshop (IIPHDW), 117–122, doi: [10.1109/IIPHDW.2018.8388338](https://doi.org/10.1109/IIPHDW.2018.8388338)
- Miller, W. C., & Merrill, P. W. 1951, ApJ, 113, 624, doi: [10.1086/145430](https://doi.org/10.1086/145430)
- Moffat, A. F. J., Marchenko, S. V., Seggewiss, W., et al. 1998, A&A, 331, 949
- . 1999, A&A, 345, 321
- Mohr-Smith, M., Drew, J. E., Napiwotzki, R., et al. 2017, MNRAS, 465, 1807, doi: [10.1093/mnras/stw2751](https://doi.org/10.1093/mnras/stw2751)
- Morgan, W. W., Code, A. D., & Whitford, A. E. 1955, ApJS, 2, 41, doi: [10.1086/190016](https://doi.org/10.1086/190016)
- Negueruela, I., & Schurch, M. P. E. 2007, A&A, 461, 631, doi: [10.1051/0004-6361:20066054](https://doi.org/10.1051/0004-6361:20066054)
- Neiner, C., de Batz, B., Cochard, F., et al. 2011, AJ, 142, 149, doi: [10.1088/0004-6256/142/5/149](https://doi.org/10.1088/0004-6256/142/5/149)
- Paszke, A., Gross, S., Massa, F., et al. 2019, Advances in neural information processing systems, 32, 8026. <https://arxiv.org/abs/1912.01703>
- Pérez-Ortiz, M. F., García-Varela, A., Quiroz, A. J., Sabogal, B. E., & Hernández, J. 2017, A&A, 605, A123, doi: [10.1051/0004-6361/201628937](https://doi.org/10.1051/0004-6361/201628937)

- Peters, G. J., Gies, D. R., Grundstrom, E. D., & McSwain, M. V. 2008, *ApJ*, 686, 1280, doi: [10.1086/591145](https://doi.org/10.1086/591145)
- Peters, G. J., Pewett, T. D., Gies, D. R., Touhami, Y. N., & Grundstrom, E. D. 2013, *ApJ*, 765, 2, doi: [10.1088/0004-637X/765/1/2](https://doi.org/10.1088/0004-637X/765/1/2)
- Peters, G. J., Wang, L., Gies, D. R., & Grundstrom, E. D. 2016, *ApJ*, 828, 47, doi: [10.3847/0004-637X/828/1/47](https://doi.org/10.3847/0004-637X/828/1/47)
- Portegies Zwart, S. F. 2000, *ApJ*, 544, 437, doi: [10.1086/317190](https://doi.org/10.1086/317190)
- Poveda, A., Ruiz, J., & Allen, C. 1967, *Boletín de los Observatorios Tonantzintla y Tacubaya*, 4, 86
- Quirrenbach, A., Bjorkman, K. S., Bjorkman, J. E., et al. 1997, *ApJ*, 479, 477, doi: [10.1086/303854](https://doi.org/10.1086/303854)
- Recht, B., Roelofs, R., Schmidt, L., & Shankar, V. 2018, arXiv e-prints, arXiv:1806.00451. <https://arxiv.org/abs/1806.00451>
- Reed, B. C. 2003, *AJ*, 125, 2531, doi: [10.1086/374771](https://doi.org/10.1086/374771)
- Reig, P. 2011, *Ap&SS*, 332, 1, doi: [10.1007/s10509-010-0575-8](https://doi.org/10.1007/s10509-010-0575-8)
- Ren, J.-J., Wu, H., Wu, C.-J., et al. 2021, *Research in Astronomy and Astrophysics*, 21, 051, doi: [10.1088/1674-4527/21/3/51](https://doi.org/10.1088/1674-4527/21/3/51)
- Richardson, N. D., Thizy, O., Bjorkman, J. E., et al. 2021, *MNRAS*, 508, 2002, doi: [10.1093/mnras/stab2759](https://doi.org/10.1093/mnras/stab2759)
- Rivinius, T., Carciofi, A. C., & Martayan, C. 2013, *A&A Rv*, 21, 69, doi: [10.1007/s00159-013-0069-0](https://doi.org/10.1007/s00159-013-0069-0)
- Schönrich, R., Binney, J., & Dehnen, W. 2010, *MNRAS*, 403, 1829, doi: [10.1111/j.1365-2966.2010.16253.x](https://doi.org/10.1111/j.1365-2966.2010.16253.x)
- Semaan, T., Gutiérrez-Soto, J., Frémat, Y., et al. 2013, in *Astrophysics and Space Science Proceedings*, Vol. 31, *Stellar Pulsations: Impact of New Instrumentation and New Insights*, ed. J. C. Suárez, R. Garrido, L. A. Balona, & J. Christensen-Dalsgaard, 261, doi: [10.1007/978-3-642-29630-7\\_47](https://doi.org/10.1007/978-3-642-29630-7_47)
- Semaan, T., Martayan, C., Frémat, Y., et al. 2011, in *Active OB Stars: Structure, Evolution, Mass Loss, and Critical Limits*, ed. C. Neiner, G. Wade, G. Meynet, & G. Peters, Vol. 272, 547–548, doi: [10.1017/S1743921311011409](https://doi.org/10.1017/S1743921311011409)
- Shao, Y., & Li, X.-D. 2014, *ApJ*, 796, 37, doi: [10.1088/0004-637X/796/1/37](https://doi.org/10.1088/0004-637X/796/1/37)
- Shorten, C., & Khoshgofaar, T. M. 2019, *Journal of Big Data*, 6, 1, doi: [10.1186/s40537-019-0197-0](https://doi.org/10.1186/s40537-019-0197-0)
- Shridharan, B., Mathew, B., S, N., et al. 2021, arXiv e-prints, arXiv:2108.08025. <https://arxiv.org/abs/2108.08025>
- Skiff, B. A. 2014, *VizieR Online Data Catalog*, B/mk
- Spina, L., Ting, Y. S., De Silva, G. M., et al. 2021, *MNRAS*, 503, 3279, doi: [10.1093/mnras/stab471](https://doi.org/10.1093/mnras/stab471)
- Struve, O. 1931, *ApJ*, 74, 225, doi: [10.1086/143342](https://doi.org/10.1086/143342)
- Tetzlaff, N., Neuhäuser, R., & Hohle, M. M. 2011, *MNRAS*, 410, 190, doi: [10.1111/j.1365-2966.2010.17434.x](https://doi.org/10.1111/j.1365-2966.2010.17434.x)
- Vieira, R. G., Carciofi, A. C., Bjorkman, J. E., et al. 2017, *MNRAS*, 464, 3071, doi: [10.1093/mnras/stw2542](https://doi.org/10.1093/mnras/stw2542)
- Vieira, S. L. A., Corradi, W. J. B., Alencar, S. H. P., et al. 2003, *AJ*, 126, 2971, doi: [10.1086/379553](https://doi.org/10.1086/379553)
- Vioque, M., Oudmaijer, R. D., Schreiner, M., et al. 2020, *A&A*, 638, A21, doi: [10.1051/0004-6361/202037731](https://doi.org/10.1051/0004-6361/202037731)
- Štefl, S., Baade, D., Rivinius, T., et al. 2003, *A&A*, 402, 253, doi: [10.1051/0004-6361:20030224](https://doi.org/10.1051/0004-6361:20030224)
- Wang, H., Zhu, W., Guo, P., et al. 2019, *Science China Physics, Mechanics, and Astronomy*, 62, 959507, doi: [10.1007/s11433-018-9388-3](https://doi.org/10.1007/s11433-018-9388-3)
- Wang, L., Gies, D. R., & Peters, G. J. 2018, *ApJ*, 853, 156, doi: [10.3847/1538-4357/aaa4b8](https://doi.org/10.3847/1538-4357/aaa4b8)
- Wang, L., Gies, D. R., Peters, G. J., et al. 2021, *AJ*, 161, 248, doi: [10.3847/1538-3881/abf144](https://doi.org/10.3847/1538-3881/abf144)
- Wenger, M., Ochsenbein, F., Egret, D., et al. 2000, *A&AS*, 143, 9, doi: [10.1051/aas:2000332](https://doi.org/10.1051/aas:2000332)
- Witham, A. R., Knigge, C., Drew, J. E., et al. 2008, *MNRAS*, 384, 1277, doi: [10.1111/j.1365-2966.2007.12774.x](https://doi.org/10.1111/j.1365-2966.2007.12774.x)
- Wong, S. C., Gatt, A., Stamatescu, V., & McDonnell, M. D. 2016, in *2016 International Conference on Digital Image Computing: Techniques and Applications (DICTA)*, 1–6, doi: [10.1109/DICTA.2016.7797091](https://doi.org/10.1109/DICTA.2016.7797091)
- Worthey, G., Faber, S. M., Gonzalez, J. J., & Burstein, D. 1994, *ApJS*, 94, 687, doi: [10.1086/192087](https://doi.org/10.1086/192087)



- Wu, Y., Du, B., Luo, A., Zhao, Y., & Yuan, H. 2014, in *Statistical Challenges in 21st Century Cosmology*, ed. A. Heavens, J.-L. Starck, & A. Krone-Martins, Vol. 306, 340–342, doi: [10.1017/S1743921314010825](https://doi.org/10.1017/S1743921314010825)
- Wu, Y., Luo, A. L., Li, H.-N., et al. 2011, *Research in Astronomy and Astrophysics*, 11, 924, doi: [10.1088/1674-4527/11/8/006](https://doi.org/10.1088/1674-4527/11/8/006)
- Yuan, H. B., Liu, X. W., & Xiang, M. S. 2013, *MNRAS*, 430, 2188, doi: [10.1093/mnras/stt039](https://doi.org/10.1093/mnras/stt039)
- Zhang, B., Li, J., Yang, F., et al. 2021, *ApJS*, 256, 14, doi: [10.3847/1538-4365/ac0834](https://doi.org/10.3847/1538-4365/ac0834)
- Zhu, X.-P., Dai, J.-M., Bian, C.-J., et al. 2019, *Ap&SS*, 364, 55, doi: [10.1007/s10509-019-3540-1](https://doi.org/10.1007/s10509-019-3540-1)